

Examining the Source of Defects from a Mechanical Perspective for 3D Anomaly Detection

Hanzhe Liang
Shenzhen University

Aoran Wang
Shanghai AI Lab

Jie Zhou
Shenzhen University

Xin Jin
Ningbo EIT

Can Gao[†]
Shenzhen University

Jinbao Wang[†]
Shenzhen University

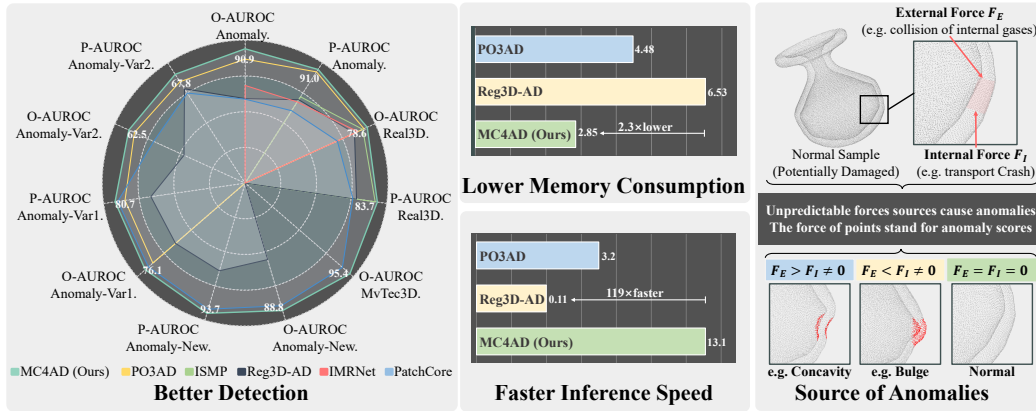


Figure 1: **Overview of our MC4AD.** Compared with existing methods, the proposed MC4AD demonstrates excellent performance, low memory, and more efficiency. We examine for the first time the source of anomalies from a mechanical perspective and use it as a motivation to design models.

Abstract

In this paper, we go beyond identifying anomalies only in structural terms and think about better anomaly detection motivated by anomaly causes. Most anomalies are regarded as the result of unpredictable defective forces from internal and external sources, and their opposite forces are sought to correct the anomalies. We introduced a Mechanics Complementary framework for 3D anomaly detection (MC4AD) to generate internal and external Corrective forces for each point. A Diverse Anomaly-Generation (DA-Gen) module is first proposed to simulate various anomalies. Then, we present a Corrective Force Prediction Network (CFP-Net) with complementary representations for point-level representation to simulate the different contributions of internal and external corrective forces. A combined loss was proposed, including a new symmetric loss and an overall loss, to constrain the corrective forces properly. As a highlight, we consider 3D anomaly detection in industry more comprehensively, creating a hierarchical quality control strategy based on a three-way decision and contributing a dataset named Anomaly-IntraVariance with intraclass variance to evaluate the model. On the proposed and existing five datasets, we obtained nine state-of-the-art performers with the minimum parameters and the fastest inference speed. The source is available at this link.

[†] Co-corresponding author. *This paper and code were done primarily by Hanzhe Liang while at Shenzhen University. For questions, please send an email to 2023362051@email.szu.edu.cn.*

1 Introduction

The task of 3D anomaly detection in industrial manufacturing requires identifying anomalies within 3D point clouds, representing structural deviations from the norm [1, 2, 3, 4]. Existing methods are mainly classified into memory bank methods and reconstruction methods [5, 6, 7]. Memory bank methods store the normal structural features into the memory bank during the training phase and judge the anomalies by comparing the structural features to be tested with the memory bank features during the testing phase [8, 9, 10, 5]. Reconstruction methods train the model to eliminate the abnormal structures and detect the anomalies by comparing the original and reconstructed structures [2, 11, 12]. However, as the motivation we illustrated in Section 2, **the existing techniques primarily focus on detecting structural features but do not account for the underlying causes of these anomalies.** This paper introduces a novel approach, the Mechanics Complementary Framework for 3D Anomaly Detection (MC4AD), which considers anomalies resulting from mechanical forces acting during production, as presented in Figure 2. These forces, including internal and external defective forces, are modeled and counteracted by corrective forces to restore the point cloud to its normal form.

We propose the Diverse Anomaly-Generation (DA-Gen) module, which simulates a range of anomalies by perturbing the surface normal vectors of 3D objects, enabling more realistic defect generation. Additionally, we present the Corrective Force Prediction Network (CFP-Net), which uses complementary representations to predict corrective forces at the point level. By applying a combined loss function consisting of a symmetric and reconstruction loss function, our approach aims to restore the affected regions of the point cloud. The model’s efficiency is further demonstrated through hierarchical quality control (HQC) strategies, designed to simulate real-world, cost-limited industrial environments. Extensive experiments on multiple datasets show that MC4AD achieves state-of-the-art detection and segmentation performance, as shown in Figure 1. We summarize the contributions:

1. We are the first to consider the causes of these anomalies from a mechanical perspective, considering most abnormalities as the action of the resultant force from internal and external defective forces, and correcting the anomalies by simulating the opposite force.
2. We propose a Mechanics Complementary Framework for 3D Anomaly Detection (MC4AD), which first creates more diverse pseudo anomalies with Diverse Anomaly-Generation, and introduces a CTF-Net that captures complementary features to predict internal and external corrective forces. A new combination of losses is proposed to provide symmetry between the internal and external corrective forces and to optimise the overall restorative results.
3. We simulate more realistic environments for industrial 3D Anomaly Detection, propose a hierarchical quality control based on the three-way decision to simulate multiple detections on real assembly lines, and make a dataset named Anomaly-IntraVariance with intra-class variance to evaluate under cost-limited conditions, which is more meaningful in real industry.
4. Extensive experiments demonstrate the effectiveness of our proposed MC4AD. We obtained 9 SOTAs with minimum parameters and fastest inference speed in detection and segmentation tests on the existing and proposed five datasets across 90 classes.

2 Preliminaries

2.1 Definition Statement

Definition A1. Given a normal sample as 3-manifold $\mathbf{M} \in \mathbb{R}^3$, which can be discretized as point cloud $P = \{\mathbf{p}_{i=1}^n\} \in \mathbb{R}^{n \times 3}$ with each point $\mathbf{p}_i = (x_i, y_i, z_i)^\top$.

Definition A2. Given a resultant defective force $F_D(\mathbf{p}) \in \mathbb{R}^3$, damaging normal object \mathbf{M} to anomalous object \mathbf{M}' , which can be decompose as a resultant external defective force $F_E(\mathbf{p}) \in \mathbb{R}^3$ and a resultant internal defective force $F_I \in \mathbb{R}^3$. These forces can be defined as

$$F_D(\mathbf{p}) = \int_M f_D(\mathbf{p}) dM = F_E(\mathbf{p}) + F_I(\mathbf{p}) = \int_{S^+} f_E(\mathbf{p}) dS^+ + \int_{S^-} f_I(\mathbf{p}) dS^-, \quad (1)$$

where $f_D(\mathbf{p})$, $f_E(\mathbf{p})$, and $f_I(\mathbf{p})$ represent the resultant defective, component external defective, and component internal defective force, respectively. S^+ and S^- stand for external and internal planes.

Definition A3. Given a resultant corrective force $F_C \in \mathbb{R}^3$, restoring anomalous object \mathbf{M}' to normal object \mathbf{M} , which can be decompose as a resultant external corrective force $F'_E \in \mathbb{R}^3$ and a resultant

internal corrective force $F_I' \in \mathbb{R}^3$. These forces can be defined as

$$\begin{aligned} F_C(\mathbf{p}) &= \int_M f_C(\mathbf{p}) dM, = F_E'(\mathbf{p}) + F_I'(\mathbf{p}) = \int_A f_E'(\mathbf{p}) dS^+ + \int_{S^-} f_I'(\mathbf{p}) dS^-, \\ &= -F_E(\mathbf{p}) - F_I(\mathbf{p}) = -F_D(\mathbf{p}) = \int_A -f_E(\mathbf{p}) dS^+ + \int_{S^-} -f_I(\mathbf{p}) dS^-, \end{aligned} \quad (2)$$

where $f_D'(\mathbf{p})$, $f_E'(\mathbf{p})$, and $f_I'(\mathbf{p})$ represent the component force, component external Corrective force, and component internal Corrective force, respectively.

Definition A4. Given a non-linear additive map $\phi : (F, G) \rightarrow \nabla G$ to represent the affect of the force F to object G , which can be defined as:

$$\begin{aligned} \mathbf{M} + \phi(F_D(\mathbf{p}), \mathbf{M}) &= \mathbf{M} + \phi(\mathbf{M}, \int_M f_D(\mathbf{p}) dM) = \mathbf{M} + \phi(\mathbf{M}, \int_{S^+} f_E(\mathbf{p}) dS^+ + \int_{S^-} f_I(\mathbf{p}) dS^-), \\ &= \mathbf{M} + \nabla \mathbf{M}_E + \nabla \mathbf{M}_I = \mathbf{M} + \nabla \mathbf{M} = \mathbf{M}', \\ \mathbf{M}' + \phi(F_C(\mathbf{p}), \mathbf{M}') &= \mathbf{M}' + \phi(\mathbf{M}', \int_{M'} f_D(\mathbf{p}) dM') = \mathbf{M}' + \phi(\mathbf{M}', \int_{S^+} f_E'(\mathbf{p}) dS^+ + \int_{S^-} f_I'(\mathbf{p}) dS^-), \\ &= \mathbf{M}' + \nabla \mathbf{M}'_E + \nabla \mathbf{M}'_I = \mathbf{M}' + \nabla \mathbf{M}' = \mathbf{M}. \end{aligned} \quad (3)$$

where $\nabla \mathbf{M} = -\nabla \mathbf{M}'$, meaning: **any object damaged by a defective force F_D can be restored by the opposite resultant Corrective force F_C , ideally.** We show the symbols used in Appendix C.

2.2 Motivation Statement

Deformation defects such as bulges, cracks, and scratches often appear on product surfaces during industrial production. This can be traced back to unexpected mechanical actions during production and transportation. **To the best of our knowledge:** Existing methods focus solely on structural anomalies without examining the causes of the anomalies, and a thorough physical analysis of the causes may lead to improved anomaly detection.

Mechanical actions include the external force $F_E(\mathbf{p})$ and internal force $F_I(\mathbf{p})$ mentioned in **Definition A2**, represented by collisions and gas expansion, respectively. The composition of defective forces $F_D(\mathbf{p})$ of external and internal forces causes defects mentioned in **Definition A2**. Anomalies arise from an imbalance in one of the internal or external forces. By simulating a composition Corrective force $F_C(\mathbf{p})$ opposite to the F_D mentioned in **Definition A3**, applying $F_D(\mathbf{p})$ to the defect, the defect will ideally be restored as mentioned in **Definition A4**. Based on the mechanical mechanism of defect formation, the conversion of the defective form \mathbf{M}' to the standard form \mathbf{M} is realized by applying the Corrective force $F_C(\mathbf{p})$, which is inverse to the defective force $F_D(\mathbf{p})$. We treat each point of the point cloud as a mechanical node subject to the defect force F_D : the theoretical force vector of a normal node should be a zero vector, while an abnormal node presents a non-zero vector. By predicting the modified force vector $F_C(\mathbf{p})$ (which is synthesized by the corresponding external force component $F_E'(\mathbf{p})$ and internal force component $F_I'(\mathbf{p})$) at each node, the mechanical influence of $F_D(\mathbf{p})$ can be reversed to cancel out, thus restoring the normal geometric characteristics of the abnormal node. The motivation is formalized as:

$$\begin{aligned} \text{Damage Source} : F_D(\mathbf{p}) &= \int_{S^+} f_E(\mathbf{p}), dS^+ + \int_{S^-} f_I(\mathbf{p}), dS^-, \\ \text{Corrective Object} : F_C(\mathbf{p}) &= \int_{S^+} f_E'(\mathbf{p}), dS^+ + \int_{S^-} f_I'(\mathbf{p}), dS^-, \\ \text{if } \mathbf{p} \text{ is normal } F_D(\mathbf{p}) &= \mathbf{0} \text{ else } \neq \mathbf{0}, F_C(\mathbf{p}) = -F_D(\mathbf{p}). \end{aligned} \quad (4)$$

where *Damage Source* and *Corrective Object* represent the potential damage at each point, and the goal of the model is to restore the damage. We further describe the theoretical implications and explain the connection to 3D anomaly detection in Appendix B.

3 Related Work

2D Anomaly Detection. In 2D anomaly detection (2D-AD), existing approaches mainly follow two paradigms: Generative and discriminative methods [13, 14, 15]. Generative methods that model

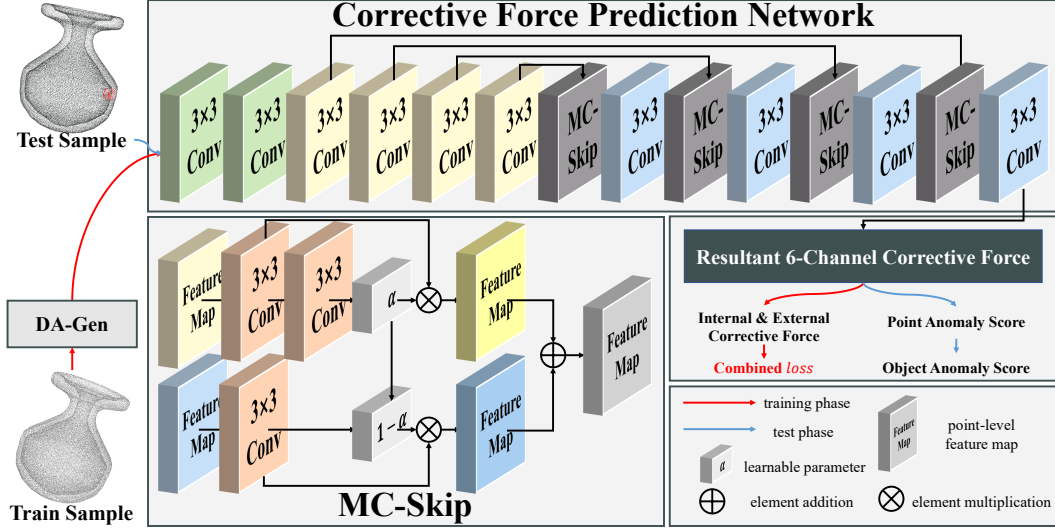


Figure 2: Overall Architecture of our MC4AD.

normal distributions using networks like Generative Adversarial Networks [16, 17], Autoencoders [18, 19] or Diffusion models [20, 21] to identify deviations, and discriminative methods that leverage supervised learning to train defect classifiers [22, 23, 24, 25, 26]. There are morphological differences between images and point clouds, and applying 2D-AD techniques directly to 3D presents challenges.

3D Anomaly Detection. 3D anomaly detection (3D-AD) aims to identify and localize anomalous points or regions within 3D point cloud data [27, 28, 29, 30]. Existing methodologies are broadly categorized into Feature Embedding-based and Reconstruction-based Methods. Feature Embedding-based Methods, including BTF [8], M3DM [31], Reg3D-AD [5], Group3AD [10], and ISMP [9], utilize pre-trained models or mathematical descriptors to extract discriminative features from normal samples. These features are aggregated into a memory bank to establish normative representations, with anomalies detected through statistical deviations between test samples and the stored feature distributions. Reconstruction-based Methods, as exemplified by IMRNet [2], R3D-AD [11], and PO3AD [12], adopt encoder-decoder architectures to compress point clouds into latent representations and reconstruct their original geometry [32, 33]. The large language model (LLM) also demonstrates anomaly detection capabilities on the ZERO-SHOT task [34, 35, 36, 37, 38, 39]. However, existing methods detect anomaly detection only from the morphological structure and never consider the source of the anomaly. This paper rethinks the source of anomalies from a mechanical perspective.

4 Methodology

4.1 Diverse Anomaly-Generation

Effective anomaly elimination in 3D models requires training with realistic pseudo-anomalies that closely resemble real defects in morphology and diversity [40, 12]. Existing 3D pseudo-anomaly generation methods are limited by their reliance on simplistic geometric patterns and cannot synthesize certain defect types, such as fine scratches. To address this limitation, we introduced Diverse Anomaly-Generation (DA-Gen) to simulate directional defective forces F_D by perturbing surface normal vectors with controlled randomness. While prior studies indicate that anomalies primarily propagate along normal directions, our method introduces slight directional deviations from these normals to enhance realism. These deviations are constrained to remain proximate to the original normal orientation. Additionally, parametric stretching is employed to control defect elongation, enabling the synthesis of narrow non-circular anomalies. Given a point cloud P , we partition it into G patches $\hat{P} = \{\hat{P}_i\}_{i=1}^G \in \mathbb{R}^{G \times K \times 3}$, where each patch contains K points sampled via a hybrid strategy combining random selection and K -nearest neighbors. The proposed DA-Gen is applied

independently to each patch \hat{P}_i , formulated as:

$$F_{D,i} = [\beta_i \cdot \lambda_i \cdot \nu_i + (1 - \lambda_i) \cdot \eta_i] \cdot \gamma_i \cdot \frac{\pi_i}{\max(\pi_i)} \cdot (1 - \sigma_i |\pi_i|). \quad (5)$$

where the subscript i represents the DA-Gen applied to the i -th patch. $\beta \in \{-1, 1\}$ dictates the displacement direction aligned with or opposing the normal vector ν , $\gamma \in [0.06, 0.12]$ specifies the maximum displacement magnitude at the anomaly center, and $\lambda \in [0.95, 1]$ governs the dominance of the normal vector ν over a randomized directional component η . The normalized projected distance π quantifies spatial attenuation of displacements, ensuring nonlinear decay from the center. The stretching parameter $\sigma \in [0, 0.08]$ inversely correlates with scratch width. Higher σ values yield narrower, more elongated anomalies. Generated samples are reported in Appendix F.3.

4.2 Corrective Force Prediction Network

Based on the motivation in Section 2, we propose the Corrective Force Prediction Network (CFP-Net), which estimates internal and external corrective forces. Since defective forces constitute continuous vector fields in physical space, our differentiable U-Net architecture explicitly preserves this continuity through its topology. **By U-Net’s universal approximation capability for inverse physical processes, this design directly enables learning implicit defective forces from point clouds and predicting correction forces through rigorous inverse modeling, where its differentiable operators inherently maintain continuous force field embeddings.** More analysis of CFP-Net to generate damaging forces and corrective forces is reported in Appendix B.3.

Our CFP-Net self-adaptively assigns the mechanical contribution of different direction forces in multi-level features by dynamically modulating the complementary feature mechanism. Specifically, our model consists of three modules: an Encoder for extracting potential mechanical features, a Bottleneck for further transforming potential features to target features, and a Decoder for reducing the dimensionality to the effective feature space. Multiple mechanical complementary skip connections (MC-Skip) are included between the Encoder and Decoder to learn the potential mechanical features. We use Conv_i to represent i -th convolutional layer from MinkUNet [41].

Given the $P = \{\mathbf{p}_{i=1}^n\} \in \mathbb{R}^{n \times 3}$ mentioned in Section 2, which employ the map φ to voxelize as $V \in \mathbb{R}^{n_v \times 3}$ ($n_v \leq n$) and the n_v stands for the voxels number. The Encoder can be formalized as:

$$F_1 = \text{Conv}_1(\varphi(P)), F_1 \in \mathbb{R}^{n_v \times C_1}, \quad (6)$$

where Conv_1 is two convolutional layers used to map the original point cloud P into C_1 -dimensional features F_1 , capturing the differential characterization $F_D(\mathbf{p}) = \int_A f_E(\mathbf{p}), dA + \int_{A'} f_I(\mathbf{p}), dA'$ of potential continuous damage source at the point level mentioned in Section 2.

The features F_1 are further processed by a Bottleneck consisting of four convolutional layers to further transform the features to the target feature domain, which can be formalized as:

$$F_i = \text{Conv}_i(F_{i-1}), F_i \in \mathbb{R}^{n_v \times C_1}, \text{ for } i \in \{2, 3, 4, 5\}, \quad (7)$$

where three convolutional layers project C_1 -dimensional features into isomorphic spaces with preserved dimensionality but distinct representations, aligning with the target feature domain.

Establishing dynamic complementary feature learning via Decoder cross-layer integration, where the hierarchical features of the bottleneck are adaptively synthesized with MC-Skip, formulated as:

$$F_{11-i} = \text{Conv}_{10-i}(\alpha_j * \text{Conv}_{j,1}(F_{10-i}) + (1 - \alpha_j) * \text{Conv}_{j,2}(F_{i-1})), F_{11-i} \in \mathbb{R}^{n_v \times C_{j+1}}, \\ \alpha_j = \text{Conv}_{j,3}(\text{Conv}_{j,2}(F_{i-1})), \alpha \in \mathbb{R}^{n_v \times 1}, \text{ for } i \in \{5, 4, 3, 2\}, j \in \{1, 2, 3, 4\}, \quad (8)$$

where α denotes a learnable complementary parameter to balance the different contributions by internal and external features, and the $\text{Conv}_{j,1}$ and $\text{Conv}_{j,2}$ are used to project features to the same feature space. The model generates a feature $F_9 \in \mathbb{R}^{n_v \times C_9}$ with external and internal coupling characteristics, and the final feature F_9' is assigned to each original point by voxel indexing.

We employ Multilayer Perceptrons (MLPs) to transform the point-level features F_9' , which contain complementary information, into internal and external corrective force vectors that are formalized as:

$$F_C = \text{MLPs}(F_9'). F_C \in \mathbb{R}^{n \times 6}. \quad (9)$$

where the F_C represents the resultant corrective force mentioned in Section 2, which is decomposed into $F'_E \in \mathbb{R}^{n \times 3}$ and $F'_I \in \mathbb{R}^{n \times 3}$, representing the external and internal corrective forces, respectively.

Anomaly Score during Inference. The norm of point-level corrective resultant force F_C is directly considered as an anomaly score during the inference phase. This is attributed to **Definition A2** in Section 2 that the model gives each point a corrective force that is a zero vector when the point is normal and a non-zero vector when it is abnormal, as described in Eq. 4. The maximum value of the point-level score is considered to be the sample-level score.

4.3 Prediction Loss

To enhance the reconstruction accuracy of corrective force fields, we propose a composite loss function that integrates three components: a symmetry loss derived from the physical constraint in Eq. 4 requiring opposing directions between internal and external correction forces in anomalous regions, a distance loss and a directional consistency loss to jointly optimize global restoration performance. The combinatorial loss function \mathcal{L}_{comb} is defined:

$$\begin{aligned} \mathcal{L}_{comb} &= \mathcal{L}_{dist} + \mathcal{L}_{dir} + \mathcal{L}_{sym}, \\ &= \frac{1}{N} \sum_{i=1}^N \left(\frac{\|F'_{I,i} - F'_{E,i}\|_1}{\|F'_{I,i}\|_2 + \|F'_{E,i}\|_2 + \epsilon} - \frac{F'_{I,i}}{\|F'_{I,i}\|_2 + \epsilon} \cdot \frac{F'_{E,i}}{\|F'_{E,i}\|_2 + \epsilon} \right) \\ &\quad + \frac{1}{N} \sum_{i=1}^N \|F_{D,i} - F_{C,i}\| - \frac{1}{N} \sum_{i=1}^N \frac{F_{D,i}}{\|F_{D,i}\|_2 + \epsilon} \cdot \frac{F_{C,i}}{\|F_{C,i}\|_2 + \epsilon}. \end{aligned} \quad (10)$$

where the subscript $i \in \{1, \dots, N\}$ denotes the i -th point in the point cloud and ϵ is set to $1e-8$ to prevent division by zero. This loss enforces anti-symmetric constraints between internal and external forces, motivated by the Eq. 4: For normal points, the resultant corrective force F_C should approximate the zero vector, whereas anomalous points exhibit non-zero resultant forces with complementary force pairs maintaining $\|F'_{E,i}\|_2 = \|F'_{I,i}\|_2$. The distance loss \mathcal{L}_{dist} and the directional consistency loss \mathcal{L}_{dir} to optimize global restoration performance help the model allocate more attention to the anomalous structures. The combined loss \mathcal{L}_{comb} was used to constrain the overall reconstruction while satisfying our mechanical motivation with the reconstruction effect.

4.4 3D Anomaly Detection in Industry

Quality Control (QC) under cost limitations is an important topic in real industrial scenarios [42]. Enterprises often encounter the following two scenarios in real manufacturing: **S1**: Multi-level QC is an essential part of the QC landscape, and it is a common strategy to use coarse QC to detect significantly normal samples and then fine QC to identify anomalies in subtle samples. **S2**: Moreover, the number of different subcategories of products produced for the same series of products can be changed by the economics of market demand. Using an assembly line to produce different subcategories of products is a common strategy within cost limitations.

To further simulate the real industrial manufacturing, we first propose a hierarchical quality control (HQC) based on a three-way decision by simplifying our model to form a pruned version, which is collocated with our original method to realize the multilevel quality control mentioned in **S1**. In addition, a dataset named Anomaly-IntraVariance with multiple subcategories is proposed for evaluating the performance of the model in the **S2**. Information on the dataset is briefly described in Section 5.1 and discussed in detail in the Appendix D.

We implement a two-stage hierarchical detection framework through aggressive model compression: (1) The Bottleneck layers are reduced from three convolutional blocks to two, and the Decoder from four to two blocks, achieving 60% parameter reduction (2) During inference, the compressed model V_P computes pruning scores $S_P = \{s_i\}_{i=1}^N$ following Section 4.2, where samples with $s_i \in \text{Top-}b\%(S_P)$ are classified as normal via thresholding in **S1**. The remaining $(1 - b\%)$ samples undergo full analysis by the original model V_O , formalized as:

$$\begin{cases} \mathcal{D}_{\text{normal}} = \{P_i \mid \text{rank}(s_i) \leq bN, s_i = V_P(P_i)\}, \\ \mathcal{D}_{\text{test}} = V_O(\{P_i\} \setminus \mathcal{D}_{\text{normal}}). \end{cases} \quad (11)$$

Table 1: O-AUROC performance of different methods on Anomaly-ShapeNet, where best and second-place results are highlighted in **red** and **blue**, respectively. The full version is in Appendix G

O-AUROC																	
Method	ashtay0	bag0	bottle	bowl	bucket	cap	cup	eraser	headset	helmet	jar	micro	shelf	tap0	vase0	Average	Mean Rank
BTF(Raw)	0.578	0.410	0.558	0.470	0.469	0.554	0.462	0.525	0.447	0.501	0.420	0.563	0.164	0.549	0.517	0.493	8.73
BTF(FPFH)	0.420	0.546	0.404	0.581	0.517	0.553	0.598	0.719	0.505	0.611	0.424	0.671	0.609	0.553	0.464	0.528	8.03
M3DM	0.577	0.537	0.584	0.579	0.405	0.586	0.548	0.627	0.597	0.525	0.441	0.357	0.564	0.747	0.534	0.552	7.83
PatchCore(FPFH)	0.587	0.571	0.614	0.558	0.510	0.597	0.593	0.657	0.610	0.485	0.472	0.388	0.494	0.760	0.554	0.568	7.35
PatchCore(PointMAE)	0.591	0.601	0.588	0.547	0.577	0.597	0.583	0.677	0.609	0.518	0.483	0.488	0.523	0.498	0.582	0.562	7.40
CPMF	0.353	0.643	0.469	0.679	0.542	0.568	0.498	0.689	0.551	0.535	0.610	0.509	0.685	0.528	0.514	0.559	7.35
Reg3D-AD	0.597	0.706	0.569	0.548	0.681	0.687	0.524	0.343	0.574	0.532	0.592	0.414	0.688	0.659	0.576	0.572	7.45
IMRNet	0.671	0.660	0.631	0.676	0.676	0.721	0.700	0.548	0.698	0.613	0.780	0.755	0.603	0.686	0.629	0.661	4.95
R3D-AD	0.833	0.720	0.750	0.751	0.720	0.744	0.767	0.890	0.767	0.703	0.838	0.762	0.696	0.818	0.734	0.749	3.23
PO3AD	1.000	0.833	0.920	0.883	0.820	0.843	0.852	0.995	0.866	0.864	0.866	0.776	0.573	0.713	0.826	0.839	2.35
Ours	1.000	0.976	0.971	0.943	0.922	0.876	0.964	1.000	0.937	0.930	0.914	0.924	0.696	0.786	0.889	0.909	1.08

where $\text{rank}(s_i)$ denotes the ascending order ranking of pruning scores. Moreover, this HQC can be generalised to the memory bank approach. We describe how to generalise HQC to the memory bank approach and details about the pruned version in Appendix A.4 and A.5.

5 Experiment

5.1 Implementation

Datasets. (1) The **Anomaly-ShapeNet** [2] has over 1,600 positive and negative samples from 40 categories, leading to a more challenging setting due to the large number of categories. (2) The **Anomaly-ShapeNet-New** [2] provides over 450 positive and negative samples crossing 12 categories, which is not been used as an evaluation dataset before. (3) The **MvTec3D-AD** [43] includes 4,147 RGB-D sample pairs from 10 categories, of which 894 are anomalous. We use the depth sample for detection evaluation. (4) The **Real3D-AD** [5] dataset consists of 1,254 large-scale, high-resolution point cloud samples from 12 categories, with the training set for each category only containing 4 normal samples. (5) We introduce the **Anomaly-IntraVariance** dataset, the first 3D dataset for simulating real-world production situations where an assembly line produces multiple products, and contains more than 1,000 samples from 16 categories. We report more details in the Appendix D.

Baselines. We selected BTF [8], PatchCore [22], M3DM [31], CPMF [44], Reg3D-AD [5], IMRNet [2], R3D-AD [11], ISMP [9] and PO3AD [12] for comparison. We evaluate the excellent performance of these models on Anomaly-ShapeNet-New. We report experimental Details, how we chose baselines, and how we implemented baselines in Appendix A.1, A.2, and A.3, respectively.

Evaluation Metrics. We adopted Point-Level Area Under the Receiver Operator Curve (P-AUROC, \uparrow) and Point-Level Area Under the Per-Region-Overlap (P-AUPR, \uparrow) to evaluate pixel-level anomaly segmentation precision and Object-Level Area Under the Receiver Operator Curve (O-AUROC, \uparrow) and Object-Level Area Under the Per-Region-Overlap (O-AUPR, \uparrow) to evaluate object-level anomaly detection performance. The *Mean Ranking* (\downarrow) is also used for evaluation to avoid a small number of categories dominating the average performance. Frames Per Second (FPS, \uparrow) and Parameters (\downarrow) are introduced to evaluate the inference speed and size of methods.

5.2 Comparison Experiment

Comparison on Anomaly-ShapeNet. Tables 10 and 11 provide the detection and segmentation results of different methods on Anomaly-ShapeNet across 40 categories, respectively. The proposed approach obtained an outstanding average O-AUROC and P-AUROC of 90.9% and 91.0%, outperforming the second-best methods by 7.0% and 1.2%, respectively. Moreover, our method reaches 94.0% of the average results and outperforms the second-best methods by 5.9%. Notably, our method achieved the best average ranking on O-AUROC, P-AUROC, and O-AURP, demonstrating that our approach outperforms our competitors in most categories.

Comparison on Anomaly-ShapeNet-New. Tables 14 and 13 provide the detection and segmentation results of different methods on Anomaly-ShapeNet-New across 12 categories. The MC4AD obtained an outstanding average O-AUROC and P-AUROC of 88.8% and 93.7%, respectively.

Comparison on MvTec3D-AD. Table 15 provides the detection and segmentation results of different only-3D methods on MvTec3D-AD across 12 categories, respectively. The proposed approach obtained an outstanding average O-AUROC and P-AUROC of 95.4% and 94.6%, outperforming the

Table 2: Ablation and Parameter Sensitivity Experiments.

Method	V_1	V_2	V_3	V_4	V_P	V_O	Method	O-AUROC	P-AUROC	FPS
\mathcal{L}_{sym}	-	✓	✓	✓	✓	✓	<i>w/o GMR</i>	0.733	0.740	17.1
\mathcal{L}_{dir}	✓	-	✓	✓	✓	✓	<i>Out = 3</i>	0.746	0.795	14.8
\mathcal{L}_{dist}	✓	✓	-	✓	✓	✓	<i>Layer₂</i>	0.728	0.713	18.2
\mathcal{A}_R	✓	✓	✓	-	✓	✓	<i>Layer₄</i>	0.763	0.766	16.6
O-AUROC	0.652	0.678	0.702	0.764	0.754	0.786	<i>Layer₆</i>	0.780	0.802	16.0
P-AUROC	0.688	0.705	0.733	0.812	0.792	0.837	<i>Layer₈</i>	0.786	0.837	14.8

previous method, such as M3DM of 94.5% and 90.6%. This may be attributed to capitalizing on the reason for manufacturing process anomalies to capture structural anomalies.

Comparison on Real3D-AD. Tables 18 and 17 present the detection and segmentation results of different methods on Real3D-AD across 12 categories, respectively. Our model obtained O-AUROC and P-AUROC of 78.6% and 83.7%, respectively, maintaining excellent segmentation performance while achieving the detection performance of SOTA. This may be attributed that the model predicts better when the training set and testing set vary significantly.

Comparison on Anomaly-IntraVariance. Tables 19 present the detection and segmentation results of different methods on Anomaly-IntraVariance across 16 categories, where Group 1 includes two subspecies and Group 2 has four subspecies. Our model achieves 76.1% and 80.7% on Group 1 and obtains 62.5% and 67.8% on the more challenging Group 2. The average abnormal detection metrics performed 4.40% and 2.65% better than the second-best method.

5.3 Ablation and Parameter Sensitivity Experiments

We conducted extensive experiments on Real3D-AD across 12 categories, as shown in Table 2.

Analysis of multiple loss functions effectiveness. “ V_1 ” is to predict a point cloud that lacks symmetry constraints, resulting in a predicted imbalance of internal and external Corrective forces. Without \mathcal{L}_{sym} , the O-AUROC and P-AUROC decreased by 13.4% and 14.9%, respectively, which may be attributed to the force imbalance resulting in an incorrect offset to the normal point. Moreover, we designed “ V_2 ”, where the model is supervised without \mathcal{L}_{dir} . The performance causes a degradation of the 10.8% and 13.2% anomaly detection metrics because the direction of the incorrect force is not constrained, resulting in the direction of the offset not being taken into account in the prediction of the offset. Analogous to “ V_2 ”, “ V_3 ” is proposed for constraining the correct size of the offset. The model performs 8.4% and 10.4% decrease in O-AUROC and P-AUROC, respectively, which may be attributed that the model meets challenges to learn the offset distance for both normal and pseudo-abnormal points without \mathcal{L}_{dist} . Therefore, all the proposed loss functions are crucial for predicting the incorrect force and thereby correctly predicting the corrective forces.

Analysis of modules effectiveness. In “ V_4 ” it is observed that O-AUROC and P-AUROC are reduced by 2.2% and 2.5%, respectively, due to the replacement of our proposed anomaly generation with Norm-AS in PO3AD, which decreases the learned diversity of anomalies, and thus leads to a decrease in anomaly detection performance. In addition, our pruned version of “ V_P ” acquires a more efficient 20 FPS (>14.8 FPS) while maintaining excellent anomaly detection performance, making our DMD strategy potentially possible, as discussed in Section 5.4. Moreover, the model without GMR (*w/o GMR*) modules failed to capture the complementary features of external and internal Corrective forces and was not able to generate the resultant Corrective force, resulting in a decrease in the anomaly detection metrics by 5.3% and 9.7%, respectively. In contrast, the model directly outputs 3-channel offsets (*Out = 3*) equivalent to the direct learning of the Corrective force, resulting in a decrease of 4.0% and 4.2% in P-AUROC and O-AUROC, respectively. More discussion about the use of the Corrective force is reported in Section 5.5. We finally evaluated the effectiveness of each layer and observed that the number of layers was reduced from 8 to 2, and 5.8% and 12.4% reduced the positive correlation of anomaly

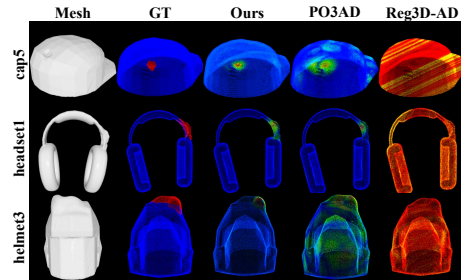


Figure 3: Qualitative results of localization.

Table 3: Comparison between One Model and our DMD.

Method	Anomaly-ShapeNet						Real3D-AD					
	One Model			DMD			One Model			DMD		
	O-AUROC	P-AUROC	FPS	O-AUROC	P-AUROC	FPS	O-AUROC	P-AUROC	FPS	O-AUROC	P-AUROC	FPS
BTF	0.528	0.628	4.8	0.543	0.784	6.0 (1.2 ↑)	0.603	0.733	2.5	0.602	0.735	3.4 (0.9 ↑)
M3DM	0.552	0.616	1.9	0.556	0.617	2.2 (0.3 ↑)	0.552	0.631	1.0	0.584	0.632	1.5 (0.5 ↑)
Reg3D-AD	0.572	0.668	1.4	0.588	0.704	1.9 (0.5 ↑)	0.704	0.705	0.8	0.709	0.712	1.6 (0.8 ↑)
ISMP	0.698	0.691	1.3	0.698	0.718	2.0 (0.6 ↑)	0.767	0.836	0.7	0.765	0.845	1.4 (0.5 ↑)
Ours	0.909	0.910	25.0	0.909	0.910	26.4 (1.4 ↑)	0.786	0.837	14.8	0.790	0.837	15.7 (0.9 ↑)

Table 4: Results of Generalizability Experiments and Efficiency Analysis.

Method	Classification [49]		Segmentation [50]		Datasets	Training		Inference	
	w/o normal	with normal	Instance IoU	Class IoU		Frame	Memory	Frame	Memory
PointNet	89.2	90.6	83.7	80.4	Anomaly-ShapeNet (PO3AD)	8.3	5.1	3.4	3.2
PointNet(Ours)	90.1 (0.9 ↑)	91.4 (0.8 ↑)	84.8 (1.1 ↑)	81.0 (0.6 ↑)	Anomaly-ShapeNet (Ours)	30.1 (21.8 ↑)	2.5 (2.6 ↓)	28.4 (25.0 ↑)	1.3 (1.9 ↓)
PointNet++	91.9	92.2	85.1	81.9	Anomaly-ShapeNet-New (PO3AD)	14.2	3.1	10.8	2.8
PointNet++(Ours)	92.4 (0.5 ↑)	92.4 (0.2 ↑)	85.9 (0.8 ↑)	82.6 (0.7 ↑)	Anomaly-ShapeNet-New (Ours)	45.5 (31.3 ↑)	2.2 (0.9 ↓)	28.1 (17.3 ↑)	2.1 (0.7 ↓)
PointTransformer	93.7	93.9	86.6	83.7	Mvtec3D-AD (AST)	49.0	11.8	50.4	5.8
PointTransformer(Ours)	94.1 (0.4 ↑)	94.4 (0.5 ↑)	87.0 (0.4 ↑)	84.4 (0.7 ↑)	Mvtec3D-AD (Ours)	50.6 (1.6 ↑)	3.9 (7.9 ↓)	50.8 (0.4 ↑)	1.9 (3.9 ↓)
DGCNN	93.3	93.9	85.1	82.3	Real3D-AD (PO3AD)	7.6	6.8	3.2	5.4
DGCNN(Ours)	94.1 (0.8 ↑)	94.8 (0.9 ↑)	85.9 (0.8 ↑)	83.0 (0.7 ↑)	Real3D-AD (Ours)	15.3 (7.7 ↑)	4.4 (2.4 ↓)	13.1 (9.9 ↑)	2.9 (2.5 ↓)

(a) Generalization on Classical Models.

(b) Resource Utilization.

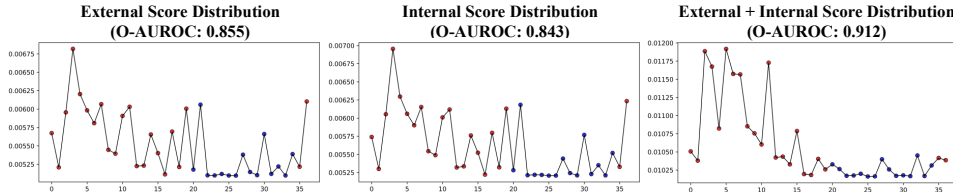


Figure 4: The distribution of anomaly detection scores on class “vase9”, compared between External, Internal, and Internal+External. Red and blue represent abnormal and normal points, respectively.

detection metrics. To balance performance and efficiency, we choose 8 layers for the experiments. More parameter sensitivity experiments are reported in the Appendix E.

5.4 Generalizability Experiments and Resource Analysis

Generalizability Experiments. We apply MC-Skip to the time-tested classical model, including PointNet [45], PointNet++ [46], PointTransformer [47], and DGCNN [48], to validate the generalizability of our model. As shown in Table 4a, the accuracies with and without normal participation on the classification task [49] increased on average by 0.65% and 0.6%, respectively, and the instance average IoU and class average IoU on the segmentation task [50] increased on average by 0.775% and 0.675%, respectively. Moreover, our DMD strategy performs well on existing 3D anomaly detection models and generalizes to memory bank, as reported in Table 3. Our approach resulted in 10.3% and 15.3% FPS average inference rate improvements on Anomaly-ShapeNet and Real3D-AD, respectively, across a representative variety of methods. Implementation details are shown in Appendix A.6.

Resource Analysis. As shown in Table 4b, we report the resource consumption on different datasets and compare it with the model that consumes the minimum resources. Our model balances memory consumption and efficiency while maintaining SOTA performance. In the four datasets available, our rates at training and testing were improved by an average of 15.6 FPS and 13.15 FPS, respectively, compared to the most efficient models available. They only took an average memory of 3.25 GB and 2.075 GB during training and testing, respectively. This may be attributed to the fewer parameters of **only 14 M**, which results significant reduction compared to the PO3AD (34 M). Our model is the preferred choice in industrial anomaly detection with lower memory and a more efficient method.

5.5 Benefit of Combining External&Internal Corrective Forces.

MC4AD achieves 90.9% O-AUROC by integrating bidirectional corrective forces. Figure 4 demonstrates that external-internal forces enhance anomaly discrimination by 7.0% over single-force via complementary feature extraction mechanisms. More comparisons are shown in Appendix F.1. Our model accurately segments anomalies in complex structures while assigning lower scores to normal parts, as shown in Figure 3. More results are reported in Appendix F.2.

6 Conclusion

This paper presents MC4AD, a novel 3D anomaly detection method that investigates the source of anomalies from a mechanical perspective. By considering anomalies as the result of the action of a damaging force, we repaired the anomalies utilizing a corrective force. We generate diverse anomalies by DA-Gen and obtain capture of potentially differentiable damage forces using the proposed CFP-Net to predict the corresponding corrective forces. And we guarantee the correct generation of the corrective force through new combined loss functions. Moreover, a dataset with intraclass variance named Anomaly-IntraVariance and a hierarchical quality control strategy were proposed to further simulate a real assembly line environment. Nine advanced anomaly detection and segmentation performance metrics are demonstrated in extensive comparative experiments on the proposed and existing five datasets across 90 categories. **Limitation.** MC4AD lacks explicit physical constraints to derive damage forces for future work; we discuss more in Appendix H.

References

- [1] Y. Lin, Y. Chang, X. Tong, J. Yu, A. Liotta, G. Huang, W. Song, D. Zeng, Z. Wu, Y. Wang, and W. Zhang, "A survey on rgb, 3d, and multimodal approaches for unsupervised industrial image anomaly detection," *Information Fusion*, vol. 121, p. 103139, 2025. [Online]. Available: <https://www.sciencedirect.com/science/article/pii/S156625352500212X>
- [2] W. Li, X. Xu, Y. Gu, B. Zheng, S. Gao, and Y. Wu, "Towards scalable 3d anomaly detection and localization: A benchmark via 3d anomaly synthesis and a self-supervised learning network," in *Proceedings of the IEEE/CVF Conference on Computer Vision and Pattern Recognition (CVPR)*, June 2024, pp. 22 207–22 216.
- [3] J. Liu, G. Xie, R. Chen, X. Li, J. Wang, Y. Liu, C. Wang, and F. Zheng, "Real3d-ad: A dataset of point cloud anomaly detection," in *Advances in Neural Information Processing Systems*, A. Oh, T. Naumann, A. Globerson, K. Saenko, M. Hardt, and S. Levine, Eds., vol. 36. Curran Associates, Inc., 2023, pp. 30 402–30 415. [Online]. Available: https://proceedings.neurips.cc/paper_files/paper/2023/file/611b896d447df43c898062358df4c114-Paper-Datasets_and_Benchmarks.pdf
- [4] Y. Jing, W. Lin, B. Sheil, and S. Acikgoz, "A 3D Multimodal Feature for Infrastructure Anomaly Detection," *arXiv e-prints*, p. arXiv:2502.05779, Feb. 2025.
- [5] J. Liu, G. Xie, X. Li, J. Wang, Y. Liu, C. Wang, F. Zheng *et al.*, "Real3d-ad: A dataset of point cloud anomaly detection," in *Thirty-seventh Conference on Neural Information Processing Systems Datasets and Benchmarks Track*, 2023.
- [6] X. Cao, C. Tao, and J. Du, "Deep subspace learning for surface anomaly classification based on 3d point cloud data," 2025. [Online]. Available: <https://arxiv.org/abs/2502.11669>
- [7] J. Liao, X. Xu, Y. Su, R.-C. Tu, Y. Liu, D. Tao, and X. Yang, "Robust distribution alignment for industrial anomaly detection under distribution shift," 2025. [Online]. Available: <https://arxiv.org/abs/2503.14910>
- [8] E. Horwitz and Y. Hoshen, "Back to the feature: Classical 3d features are (almost) all you need for 3d anomaly detection," 2022. [Online]. Available: <https://arxiv.org/abs/2203.05550>
- [9] H. Liang, G. Xie, C. Hou, B. Wang, C. Gao, and J. Wang, "Look inside for more: Internal spatial modality perception for 3d anomaly detection," 2025. [Online]. Available: <https://arxiv.org/abs/2412.13461>
- [10] H. Zhu, G. Xie, C. Hou, T. Dai, C. Gao, J. Wang, and L. Shen, "Towards high-resolution 3d anomaly detection via group-level feature contrastive learning," in *Proceedings of the 32nd ACM International Conference on Multimedia*, ser. MM '24. ACM, Oct. 2024, p. 4680–4689. [Online]. Available: <http://dx.doi.org/10.1145/3664647.3680919>
- [11] Z. Zhou, L. Wang, N. Fang, Z. Wang, L. Qiu, and S. Zhang, "R3d-ad: Reconstruction via diffusion for 3d anomaly detection," in *European Conference on Computer Vision (ECCV)*, 2024.
- [12] J. Ye, W. Zhao, X. Yang, G. Cheng, and K. Huang, "Po3ad: Predicting point offsets toward better 3d point cloud anomaly detection," 2024. [Online]. Available: <https://arxiv.org/abs/2412.12617>

- [13] J. Liu, G. Xie, J. Wang, S. Li, C. Wang, F. Zheng, and Y. Jin, “Deep industrial image anomaly detection: A survey,” *Machine Intelligence Research*, vol. 21, no. 1, p. 104–135, Jan. 2024. [Online]. Available: <http://dx.doi.org/10.1007/s11633-023-1459-z>
- [14] X. Tao, X. Gong, X. Zhang, S. Yan, and C. Adak, “Deep learning for unsupervised anomaly localization in industrial images: A survey,” *IEEE Transactions on Instrumentation and Measurement*, vol. 71, pp. 1–21, 2022.
- [15] G. Xie, J. Wang, J. Liu, J. Lyu, Y. Liu, C. Wang, F. Zheng, and Y. Jin, “Im-iad: Industrial image anomaly detection benchmark in manufacturing,” *IEEE Transactions on Cybernetics*, vol. 54, no. 5, pp. 2720–2733, 2024.
- [16] J. Song, K. Kong, Y.-I. Park, S.-G. Kim, and S.-J. Kang, “Anoseg: Anomaly segmentation network using self-supervised learning,” 2021. [Online]. Available: <https://arxiv.org/abs/2110.03396>
- [17] Y. Liang, J. Zhang, S. Zhao, R. Wu, Y. Liu, and S. Pan, “Omni-frequency channel-selection representations for unsupervised anomaly detection,” *arXiv preprint arXiv:2203.00259*, 2022.
- [18] X. Tao, D. Zhang, W. Ma, Z. Hou, Z. Lu, and C. Adak, “Unsupervised anomaly detection for surface defects with dual-siamese network,” *IEEE Transactions on Industrial Informatics*, vol. 18, no. 11, pp. 7707–7717, 2022.
- [19] T. Liu, B. Li, X. Du, B. Jiang, L. Geng, F. Wang, and Z. Zhao, “Simple and effective frequency-aware image restoration for industrial visual anomaly detection,” *Advanced Engineering Informatics*, vol. 64, p. 103064, Mar. 2025. [Online]. Available: <http://dx.doi.org/10.1016/j.aei.2024.103064>
- [20] J. Wyatt, A. Leach, S. M. Schmon, and C. G. Willcocks, “Anoddpm: Anomaly detection with denoising diffusion probabilistic models using simplex noise,” in *2022 IEEE/CVF Conference on Computer Vision and Pattern Recognition Workshops (CVPRW)*, 2022, pp. 649–655.
- [21] H. He, J. Zhang, H. Chen, X. Chen, Z. Li, X. Chen, Y. Wang, C. Wang, and L. Xie, “A diffusion-based framework for multi-class anomaly detection,” in *Proceedings of the AAAI Conference on Artificial Intelligence*, vol. 38, no. 8, 2024, pp. 8472–8480.
- [22] K. Roth, L. Pemula, J. Zepeda, B. Schölkopf, T. Brox, and P. Gehler, “Towards total recall in industrial anomaly detection,” in *2022 IEEE/CVF Conference on Computer Vision and Pattern Recognition (CVPR)*, 2022, pp. 14 298–14 308.
- [23] N. Cohen and Y. Hoshen, “Sub-image anomaly detection with deep pyramid correspondences,” 2021. [Online]. Available: <https://arxiv.org/abs/2005.02357>
- [24] K. Batzner, L. Heckler, and R. König, “Efficientad: Accurate visual anomaly detection at millisecond-level latencies,” 2024. [Online]. Available: <https://arxiv.org/abs/2303.14535>
- [25] M. Bergmann, Pauland Fauser, D. Sattlegger, and C. Steger, “Uninformed students: Student-teacher anomaly detection with discriminative latent embeddings,” in *Proceedings of the IEEE/CVF Conference on Computer Vision and Pattern Recognition (CVPR)*, June 2020.
- [26] M. Rudolph, T. Wehrbein, B. Rosenhahn, and B. Wandt, “Fully convolutional cross-scale-flows for image-based defect detection,” in *Winter Conference on Applications of Computer Vision (WACV)*, Jan. 2022. [Online]. Available: [arxiv](https://arxiv.org/abs/2110.03396)
- [27] —, “Asymmetric student-teacher networks for industrial anomaly detection,” in *Winter Conference on Applications of Computer Vision (WACV)*, Jan. 2023.
- [28] Y.-M. Chu, C. Liu, T.-I. Hsieh, H.-T. Chen, and T.-L. Liu, “Shape-guided dual-memory learning for 3d anomaly detection,” in *Proceedings of the 40th International Conference on Machine Learning*, 2023, pp. 6185–6194.
- [29] A. K. Bhunia, C. Li, and H. Bilen, “Looking 3d: Anomaly detection with 2d-3d alignment,” *CVPR*, 2024.
- [30] H. Liang, J. Zhou, X. Chen, T. Dai, J. Wang, and C. Gao, “Fence theorem: Towards dual-objective semantic-structure isolation in preprocessing phase for 3d anomaly detection,” 2025. [Online]. Available: <https://arxiv.org/abs/2503.01100>
- [31] Y. Wang, J. Peng, J. Zhang, R. Yi, Y. Wang, and C. Wang, “Multimodal industrial anomaly detection via hybrid fusion,” 2023.

- [32] Y. Liu, Y. S. Hu, Y. Chen, and J. Zelek, “Splatpose+: Real-time image-based pose-agnostic 3d anomaly detection,” 2024. [Online]. Available: <https://arxiv.org/abs/2410.12080>
- [33] M. Kruse, M. Rudolph, D. Woiwode, and B. Rosenhahn, “Splatpose & detect: Pose-agnostic 3d anomaly detection,” in *Proceedings of the IEEE/CVF Conference on Computer Vision and Pattern Recognition (CVPR) Workshops*, June 2024, pp. 3950–3960.
- [34] Y. Cao, X. Xu, C. Sun, X. Huang, and W. Shen, “Towards Generic Anomaly Detection and Understanding: Large-scale Visual-linguistic Model (GPT-4V) Takes the Lead,” *arXiv e-prints*, p. arXiv:2311.02782, Nov. 2023.
- [35] Y. Wang, K.-C. Peng, and Y. Fu, “Towards zero-shot 3d anomaly localization,” in *Proceedings of the Winter Conference on Applications of Computer Vision (WACV)*, February 2025, pp. 1447–1456.
- [36] Q. Zhou, J. Yan, S. He, W. Meng, and J. Chen, “Pointad: Comprehending 3d anomalies from points and pixels for zero-shot 3d anomaly detection,” in *Advances in Neural Information Processing Systems*, A. Globerson, L. Mackey, D. Belgrave, A. Fan, U. Paquet, J. Tomczak, and C. Zhang, Eds., vol. 37. Curran Associates, Inc., 2024, pp. 84 866–84 896. [Online]. Available: https://proceedings.neurips.cc/paper_files/paper/2024/file/9a263e235f6d1521d13a8531c7974951-Paper-Conference.pdf
- [37] Y. Cao, J. Zhang, L. Frittooli, Y. Cheng, W. Shen, and G. Boracchi, “Adaclip: Adapting clip with hybrid learnable prompts for zero-shot anomaly detection,” in *European Conference on Computer Vision*, 2024.
- [38] Y. Tang, Z. Guo, Z. Wang, R. Zhang, Q. Chen, J. Liu, D. Qu, Z. Wang, D. Wang, X. Li, and B. Zhao, “Exploring the potential of encoder-free architectures in 3d lms,” 2025. [Online]. Available: <https://arxiv.org/abs/2502.09620>
- [39] Y. Cheng, Y. Cao, G. Xie, Z. Lu, and W. Shen, “Towards zero-shot point cloud anomaly detection: A multi-view projection framework,” 2024. [Online]. Available: <https://arxiv.org/abs/2409.13162>
- [40] Y. Cheng and J. Du, “3d-pnas: 3d industrial surface anomaly synthesis with perlin noise,” 2025. [Online]. Available: <https://arxiv.org/abs/2504.12856>
- [41] C. Choy, J. Gwak, and S. Savarese, “4d spatio-temporal convnets: Minkowski convolutional neural networks,” in *Proceedings of the IEEE Conference on Computer Vision and Pattern Recognition*, 2019, pp. 3075–3084.
- [42] Y. Chen, Y. Ding, F. Zhao, E. Zhang, Z. Wu, and L. Shao, “Surface defect detection methods for industrial products: A review,” *Applied Sciences*, vol. 11, no. 16, 2021. [Online]. Available: <https://www.mdpi.com/2076-3417/11/16/7657>
- [43] P. Bergmann, X. Jin, D. Sattlegger, and C. Steger, “The mvtec 3d-ad dataset for unsupervised 3d anomaly detection and localization,” in *Proceedings of the 17th International Joint Conference on Computer Vision, Imaging and Computer Graphics Theory and Applications*. SCITEPRESS - Science and Technology Publications, 2022. [Online]. Available: <http://dx.doi.org/10.5220/0010865000003124>
- [44] Y. Cao, X. Xu, and W. Shen, “Complementary pseudo multimodal feature for point cloud anomaly detection,” *arXiv preprint arXiv:2303.13194*, 2023.
- [45] R. Q. Charles, H. Su, M. Kaichun, and L. J. Guibas, “Pointnet: Deep learning on point sets for 3d classification and segmentation,” in *2017 IEEE Conference on Computer Vision and Pattern Recognition (CVPR)*, 2017, pp. 77–85.
- [46] C. R. Qi, L. Yi, H. Su, and L. J. Guibas, “Pointnet++: Deep hierarchical feature learning on point sets in a metric space,” 2017. [Online]. Available: <https://arxiv.org/abs/1706.02413>
- [47] H. Zhao, L. Jiang, J. Jia, P. Torr, and V. Koltun, “Point transformer,” 2021. [Online]. Available: <https://arxiv.org/abs/2012.09164>
- [48] Y. Wang, Y. Sun, Z. Liu, S. E. Sarma, M. M. Bronstein, and J. M. Solomon, “Dynamic graph cnn for learning on point clouds,” *ACM Transactions on Graphics (TOG)*, 2019.
- [49] Z. Wu, S. Song, A. Khosla, F. Yu, L. Zhang, X. Tang, and J. Xiao, “3d shapenets: A deep representation for volumetric shapes,” 2015. [Online]. Available: <https://arxiv.org/abs/1406.5670>

- [50] L. Yi, V. G. Kim, D. Ceylan, I.-C. Shen, M. Yan, H. Su, C. Lu, Q. Huang, A. Sheffer, and L. Guibas, “A scalable active framework for region annotation in 3d shape collections,” *SIG-GRAPH Asia*, 2016.
- [51] I. Loshchilov and F. Hutter, “Sgdr: Stochastic gradient descent with warm restarts,” 2017. [Online]. Available: <https://arxiv.org/abs/1608.03983>
- [52] Y. Cheng, Y. Cao, D. Wang, W. Shen, and W. Li, “Boosting global-local feature matching via anomaly synthesis for multi-class point cloud anomaly detection,” *IEEE Transactions on Automation Science and Engineering*, vol. 22, pp. 12 560–12 571, 2025.
- [53] X. Yu, L. Tang, Y. Rao, T. Huang, J. Zhou, and J. Lu, “Point-bert: Pre-training 3d point cloud transformers with masked point modeling,” in *Proceedings of the IEEE Conference on Computer Vision and Pattern Recognition (CVPR)*, 2022.
- [54] K. He, X. Zhang, S. Ren, and J. Sun, “Deep residual learning for image recognition,” 2015. [Online]. Available: <https://arxiv.org/abs/1512.03385>
- [55] R. C. Bolles and M. A. Fischler, “A ransac-based approach to model fitting and its application to finding cylinders in range data,” in *Proceedings of the 7th International Joint Conference on Artificial Intelligence - Volume 2*, ser. IJCAI’81. San Francisco, CA, USA: Morgan Kaufmann Publishers Inc., 1981, p. 637–643.
- [56] Y. Pang, W. Wang, F. E. Tay, W. Liu, Y. Tian, and L. Yuan, “Masked autoencoders for point cloud self-supervised learning,” in *Computer Vision—ECCV 2022: 17th European Conference, Tel Aviv, Israel, October 23–27, 2022, Proceedings, Part II*. Springer, 2022, pp. 604–621.
- [57] A. H. Loc Vu-Quoc, “Deep learning applied to computational mechanics: A comprehensive review, state of the art, and the classics,” *Computer Modeling in Engineering & Sciences*, vol. 137, no. 2, pp. 1069–1343, 2023. [Online]. Available: <http://www.techscience.com/CMES/v137n2/53358>
- [58] K. Hornik, M. Stinchcombe, and H. White, “Multilayer feedforward networks are universal approximators,” *Neural Networks*, vol. 2, no. 5, pp. 359–366, 1989. [Online]. Available: <https://www.sciencedirect.com/science/article/pii/0893608089900208>
- [59] M. Terris, S. Hurault, M. Song, and J. Tachella, “Reconstruct anything model: a lightweight foundation model for computational imaging,” 2025. [Online]. Available: <https://arxiv.org/abs/2503.08915>
- [60] L. Barcellona, A. Zadaianchuk, D. Allegro, S. Papa, S. Ghidoni, and E. Gavves, “Dream to manipulate: Compositional world models empowering robot imitation learning with imagination,” in *The Thirteenth International Conference on Learning Representations*, 2025. [Online]. Available: <https://openreview.net/forum?id=3RSLW9YSgk>

Supplementary Material of “Examining Defects from a Mechanics Perspective for 3D Anomaly Detection”

A Experimental Details

A.1 Experimental Settings

Our experiments were trained on four NVIDIA A100-PCIE-40GBs and an Xeon Gold 6248R machine. The batch size was set to 32, and the initial learning rate was 0.001 and declined with a cosine annealing scheme [51]. The optimiser chosen was Adam. model test results were implemented on a machine fitted with an NVIDIA RTX3090 and a 12 vCPU Intel(R) Xeon(R) Platinum 8255C CPU. the number of anomalous blocks created by DA-Gen was 64 and λ was set to a random number within $[0.95, 1]$, σ was set to a random number within $[0, 0.08]$, γ was set to a random number within $[0.06, 0.12]$. b in HQC was set to 0.25. All samples were taken without using downsampling. All code is implemented using PyTorch.

A.2 How We Select Baseline

We select models according to their performance, and some lower-performing models are excluded from the selection. Moreover, some excellent work based on large language models has excelled in 3D anomaly detection. Considering the large amount of data they use that is difficult to access in the real industry, we compare models trained with limited data, such as migration training using PointMAE, or on local datasets, such as those trained on Real3D-AD. We state here some of the models that were not selected for comparison for this reason.

GLFM [52] uses pre-trained Vision-Language Models (VLMs) as feature extractors.

PointAD [36] employs multi-view projection is used to form 2D images, and 2D-LLM is used to acquire features.

ENEL [38] uses an end-to-end encoder-free large language model for 3D anomaly detection.

The above work is excellent, and we collected it in Arxiv or the official conference website. We discuss them in related work, and due to the task setup, we do not impose comparison experiments.

A.3 Implementation of Baselines

BTF extracts point cloud features using FPFH and creates a memory bank to determine anomalies by comparing the features to be tested with the memory bank features. We conducted comparative experiments using the results from their paper, and we measured the unreported results via the official implementation at the following link: <https://github.com/eliahuhorwitz/3D-ADS>.

PatchCore is a classical approach in 2D anomaly detection, which Real3D-AD extends to 3D anomaly detection. The paper uses different feature extractors [53, 54] to obtain features from the point cloud registered by RANSAC [55]. The code implementation is derived from the official Real3D-AD implementation, which can be acquired at the following link: <https://github.com/m-3lab/real3d-ad>.

M3DM uses PointMAE to obtain group-level features, which Real3D-AD extends to 3D-only anomaly detection. For the MvTec3D-AD detection results, we used the official implementation of M3DM, which is available at the following link: <https://github.com/nomewang/M3DM/blob>. For a 3D-only implementation of the paper, we used the Real3D-AD implementation, which can be accessed at the following link: <https://github.com/m-3lab/real3d-ad>.

CPMF uses multi-view projections to render pseudo-2D modalities and ResNet for representations as a complement to 3D features. The code is available at the link: <https://github.com/caoyunkang/CPMF>.

Reg3D-AD extracts features from the RANSAC-registered point cloud by using PointMAE [56]. We get the code from the following link: <https://github.com/m-3lab/real3d-ad>.

IMRNet eliminates potential anomalies in the point cloud by expanding PointMAE to circularly mask the reconstruction. Since its code is not open-sourced, we obtained its official paper performance through the following official repository: <https://github.com/Chopper-233/Anomaly-ShapeNet>.

R3D-AD eliminates potential anomalies in the point cloud by diffusion modelling. Since it is not open source, we get the official performance at the link: <https://arxiv.org/abs/2407.10862v1>.

ISMP obtains information about the interior of the point cloud through pseudo-modal projections as complementary information to obtain better anomaly detection, and we access the official implementation through the following link: <https://github.com/M-3LAB/Look-Inside-for-More>.

PO3AD eliminates potential anomalies from a point cloud by predicting point offsets. Its official implementation can be accessed at the following link: <https://github.com/yjnanan/PO3AD>.

A.4 Details of the HQC Generalisation to Memory Bank Methods

The core of HQC is an initial screening with a simplified version that uses its faster but slightly reduced detection performance to detect a fraction of significantly normal samples, leaving the other fraction of potentially abnormal samples for further detection using the original model. When the model is properly initialised, it speeds up detection without loss of accuracy.

Following the settings of Reg3D-AD, ISMP, and PatchCore, whose standard memory bank size is set to 10000. We simplify this by setting it to 1000 to detect anomalies according to the hierarchical detection of HQC.

A.5 Details of the Pruned Version

We reduce the convolutional layers in Encoder, Bottleneck, and Decoder represented by Eq. 6, Eq. 7, and Eq. 8 to one, two, and two, respectively. Since the number of convolutions in the bottleneck layer and the Decoder remains the same, the structure of the MC-Skip is retained as in the original version to look for potential corrupting forces in the internal and external structures.

Moreover, MinkUNet is a voxel-based sparse convolutional network. All convolutions used in our model were replaced with the convolutional layers used in MinkUnet, and we achieved standard performance by using the standard configuration from their paper, with the *voxel size* set to 0.03.

The pruned version follows the same training setup as described in Section A.1, and since the model structure is simpler compared to the original version, we adjust the initial learning rate upwards to 0.0015 to ensure faster convergence.

A.6 Details of Generalizability Experiments

According to the paper setup, PointNet++, DGCNN, and PointTransformer are based on PointNet. We first conduct generalisation experiments on PointNet, and then plug-and-play into the corresponding classical models according to their thesis settings. The representation of a point cloud P as a feature $F_{pointnet}$ by PointNet can be formalised as:

$$F_{pointnet} = Conv_3 \left(Conv_2 \left(Conv_1 (T-Net(P)) \right) \right), \quad (12)$$

Reformalised by inserting MC-Skip as

$$\begin{aligned}
F_1 &= T\text{-Net}(P), \\
F_2 &= \text{Conv}_1(F_1), \\
F_3 &= \text{Conv}_2(F_2), \\
F_4 &= \text{Conv}_3(\alpha_1 * \text{Conv}_{1,1}(F_2) + (1 - \alpha_1) * \text{Conv}_{1,2}(F_3)), \\
F_5 &= \text{Conv}_4(\alpha_2 * \text{Conv}_{2,1}(F_1) + (1 - \alpha_2) * \text{Conv}_{2,2}(F_4)), \\
\alpha_1 &= \text{Conv}_{1,3}(\text{Conv}_{1,2}(F_3)), \alpha_1 \in \mathbb{R}^{n_v \times 1}, \\
\alpha_2 &= \text{Conv}_{2,3}(\text{Conv}_{2,2}(F_4)), \alpha_2 \in \mathbb{R}^{n_v \times 1},
\end{aligned} \tag{13}$$

Based on the above formulation, the process encoded by PointTransformer using PointNet can be reformulated:

$$\begin{aligned}
\hat{P}_i, C_i &= KNN(FPS(P)), \\
\hat{F}_i &= \text{PointNet}(\hat{P}_i), \\
F_i &= \text{Attention}(\hat{F}_i, C_i).
\end{aligned} \tag{14}$$

where KNN and FPS stand for K Nearest Neighbours and Farthest Point Sampling, respectively, and are commonly used to divide a point cloud into patches. C_i and \hat{P}_i represent the center point and group points of the i -th patch divided, respectively. Each Patch is encoded using modified PointNet to get the encoded feature \hat{F}_i , and Attention is used for final features F_i representing the features of the i -th patch.

Following the modified PointNet of Eq. 13, the DGCNN inserts dynamic graph aggregation after each convolution. Moreover, PointNet++ feature extractor for multi-scale point clouds using PointNet.

B More Analysis about Motivation

In this paper, we view most of the anomalies that arise in industrial manufacturing as the combined result of internal and external damage forces. Moreover, we further elaborate on the theoretical implications of the individual formulas and relate them to 3D anomaly detection.

B.1 Analysis of Potential Continuous Damage Force and Correction Force

Continuous forces are usually expressed as integrals of force densities over a spatial distribution. Consider that mass M can be written as a product of density ρ and volume V [57]. In 3D-AD, the basic unit for detecting samples is the point cloud. Therefore, we ignore the mass density of the object, and each point can be ideally regarded as a unit density. Furthermore, as the point cloud is composed in the form of discrete points, the volume V can be approximated as a continuous surface S . The force representation in the 3D point cloud can be written:

$$\begin{aligned}
F &= \int_M f dM, \\
&= \int_V f d(\rho V), \\
&= \int_V \rho f dV, \\
&= \int_V f dV, \\
&= \int_S f dS,
\end{aligned} \tag{15}$$

where S represents the force acting uniformly on the internal and external surfaces.

Eq. 15 represents the combined action of complex resultant forces on the surface S . However, it is straightforward to make the model learn the complex potential resultant forces. Therefore, we further decompose the resultant forces to obtain the external force F_E and internal force F_I , which can be

represented as follows:

$$\begin{aligned} F_E &= \int_{S^+} f_E dS^+, \\ F_I &= \int_{S^-} f_I dS^-, \end{aligned} \tag{16}$$

where S^+ and S^- represent the external and the internal part of the surface S , respectively.

Considering the above theoretical basis, we formalise the damage force F_D and corrective forces F_C in the paper according to the internal and external decompositions in **Definition A2** and **Definition A3**, respectively.

B.2 Analysis of Different Forces to Normal Points and Anomaly Points

According to Eq. 4, the damage and corrective forces for a particular point \mathbf{p} to be judged as normal can be described as

$$\text{if } \mathbf{p} \text{ is normal } F_D(\mathbf{p}) = \mathbf{0} \text{ else } \neq \mathbf{0}, F_C(\mathbf{p}) = -F_D(\mathbf{p}), \tag{17}$$

The above equation can be fully expressed as:

$$\begin{aligned} \text{if } \mathbf{p} \text{ is normal, } F_D(\mathbf{p}) &= F_C(\mathbf{p}) = \mathbf{0}, \\ \text{if } \mathbf{p} \text{ is anomaly, } F_D(\mathbf{p}) &= -F_C(\mathbf{p}) \neq \mathbf{0}, \end{aligned} \tag{18}$$

Eq. 18 can be derived from Newton’s First Law of Motion. if the normal structure is undamaged, which means that the point is subjected to zero damaging force, and we do not need to apply a corrective force to rectify it. On the contrary, if a non-zero damage force is suffered, this means that the point is anomalous and, according to the definition in **Definition A4**, we need to apply an opposite corrective force to repair it.

B.3 Theoretical Analysis of the CFP-Net.

Since our model learns potential damage forces from the point cloud and generates corrective forces to counteract the effects of the damage forces through an inverse process. This process behaves as an asymmetric inverse process. The model is required to solve the following challenges:

Challenge A1. Inverse Process Capability: Given that the model aims to perform an inverse process, it should be adept at reconstructing corrective forces through inverse operations.

Challenge A2. Complementary Force Learning: To directly learn internal and external forces at each point and synthesize the resultant force, the model must capture the complementary nature of latent internal and external forces as mentioned in **Definition A2** and **Definition A3**, thereby generating accurate resultant corrective forces.

Challenge A3. Differentiability: Considering the continuity and differentiability of force distributions as mentioned in Appendix B, the proposed model must be differentiable to enable precise mathematical operations such as gradient-based optimization.

To address the challenges above, our model incorporates the following distinctive features:

For Challenge A1. As our model adopts a U-Net framework, it inherently satisfies two fundamental theorems:

Lemma A1 [58]. A feedforward neural network with a linear output layer and at least one hidden layer employing any "squashing" activation function can approximate any Borel measurable function from one finite-dimensional space to another with arbitrary precision, provided sufficient hidden units are available.

Lemma A2 [59]. The U-Net architecture is universally applicable for arbitrary inverse generative tasks in computer vision.

Given *Lemma A1* and *Lemma A2*, our proposed model theoretically guarantees superior performance in fitting the required inverse process.

For Challenge A2. As explicitly formulated in Eq. 8 through complementary constraints, our model employs the MC-Skip mechanism to adjust feature weights across different hierarchies dynamically.

This design guides the model to learn complementary feature representations, which are further regularized by a symmetric loss function as mentioned in Eq. 10.

For Challenge A3. Our model builds upon the differentiable Minkowski-UNet architecture with further modifications to ensure enhanced differentiability. We prove it simply by the following process.

Proposition A1

The mapping $\mathcal{F} : \mathbf{P} \mapsto \mathbf{F}_9$ is differentiable with respect to \mathbf{P} and all parameters $\{\mathbf{W}_1, \mathbf{W}_i, \mathbf{W}_{j,k}\}$.

Proof.

Convolutional Differentiability:

$$\begin{aligned} \therefore \quad \frac{\partial \text{Conv}(\mathbf{F}; \mathbf{W})}{\partial \mathbf{F}} &= \mathbf{W}, \\ \frac{\partial \text{Conv}(\mathbf{F}; \mathbf{W})}{\partial \mathbf{W}} &= \mathbf{F}, \end{aligned}$$

where holds for all encoder/bottleneck layers Conv_k ($k = 1, \dots, 5$).

Dynamic Weight Differentiability:

$$\begin{aligned} \therefore \quad \alpha_j &= \sigma(\mathbf{W}_{j,3} * (\mathbf{W}_{j,2} * \mathbf{F}_{j+1})), \\ \therefore \quad \frac{\partial \alpha_j}{\partial \mathbf{F}_{j+1}} &= \sigma'(\mathbf{W}_{j,3} * (\mathbf{W}_{j,2} * \mathbf{F}_{j+1})) \cdot (\mathbf{W}_{j,3} * \mathbf{W}_{j,2}), \end{aligned}$$

where $\sigma'(z) = \sigma(z)(1 - \sigma(z))$ is continuous.

Decoder Gradient Accumulation:

For decoder layer \mathbf{F}_{10-j} :

$$\begin{aligned} \therefore \quad \mathbf{F}_{10-j} &= \mathbf{W}_{10-j} * (\alpha_j(\mathbf{W}_{j,1} * \mathbf{F}_{6-j}) + (1 - \alpha_j)(\mathbf{W}_{j,2} * \mathbf{F}_{j+1})), \\ \therefore \quad \frac{\partial \mathbf{F}_{10-j}}{\partial \mathbf{P}} &= \alpha_j \mathbf{W}_{j,1} \frac{\partial \mathbf{F}_{6-j}}{\partial \mathbf{P}} + \left[(1 - \alpha_j) \mathbf{W}_{j,2} + \frac{\partial \alpha_j}{\partial \mathbf{F}_{j+1}} (\mathbf{W}_{j,1} \mathbf{F}_{6-j} - \mathbf{W}_{j,2} \mathbf{F}_{j+1}) \right] \frac{\partial \mathbf{F}_{j+1}}{\partial \mathbf{P}}, \end{aligned}$$

Global Differentiability:

$$\begin{aligned} \therefore \quad \frac{\partial \Phi}{\partial \mathbf{P}} &= \sum_{\text{all paths } p} \prod_{(i \rightarrow j) \in p} \frac{\partial \mathbf{F}_j}{\partial \mathbf{F}_i}, \\ \therefore \quad \text{All terms } \frac{\partial \mathbf{F}_j}{\partial \mathbf{F}_i} &= \mathbf{W}_k \text{ or fusion terms are continuous.} \end{aligned}$$

Thus \mathcal{F} is differentiable by composition of differentiable operations. □

Since the whole process is microscopic, this leads to our model being more suitable for learning potentially microscopic variables.

In conclusion, we theoretically ensure that the CFP-Net method is designed specifically to extract potential damage forces for 3D anomaly detection.

C Main Symbols

We present the main symbols used in the theoretical analysis and corresponding explanations, as shown in Table 5.

D Datasets: Anomaly-IntraVariance

D.1 Data Overview

We constructed an anomaly detection dataset with intra-class variance as shown in Figure 5. Group 1 contains eight classes, where each class has two subclasses. Group 2 also contains eight classes, where each class has four subclasses. Moreover, to more closely mimic 3D anomaly detection in a real industrial context, Group 2 has a smaller number of points and has been subjected to light noise. This is attributed to the tens of minutes required to scan a high-resolution sample such as

Table 5: Main symbols and corresponding explanations

Symbol	Explanation
\mathbf{M}	A normal sample as 3-manifold
\mathbf{M}'	A anomaly sample as 3-manifold
$P\{\mathbf{p}_{i=1}^n\} \in \mathbb{R}^{n \times 3}$	A point cloud with each point $\mathbf{p}_i = (x_i, y_i, z_i)^\top$
$F_D(\mathbf{p}) \in \mathbb{R}^3$	A resultant defective force
$F_E(\mathbf{p}) \in \mathbb{R}^3$	A resultant external defective force
$F_I \in \mathbb{R}^3$	A resultant internal defective force
$f_D(\mathbf{p}), f_E(\mathbf{p}), f_I(\mathbf{p})$	Resultant defective force, component external defective force, and component internal defective force
S^+ & S^-	External and internal planes
$F_C \in \mathbb{R}^3$	A resultant corrective force
$F'_E \in \mathbb{R}^3$	A resultant external corrective force
$F'_I \in \mathbb{R}^3$	A resultant internal corrective force
$f'_D(\mathbf{p}), f'_E(\mathbf{p}), f'_I(\mathbf{p})$	Component force, component external corrective force, and component internal corrective force
$\phi: (F, G) \rightarrow \nabla G$	A non-linear additive map representing the affect of the force F to object G
M	Mass
ρ	A product of density
V	Volume
S	A continuous surface

Table 6: Statistical Data of Group 1.

Statistical Data											
class	subcategories	template	positive	hole	bulge	concavity	crack	broken	scratch	bending	total
bottle	2	4	30	2	14	14	1	2	\	\	67
bowl	2	4	30	\	14	14	\	\	8	\	70
bucket	2	4	30	4	14	14	4	4	2	\	76
cap	2	4	30	4	14	14	\	4	\	1	71
cup	2	4	30	\	14	14	\	\	\	\	62
helmet	2	4	30	2	14	14	2	2	1	2	71
microphone	2	4	30	\	14	14	\	\	\	\	62
tap	2	4	30	4	14	14	2	4	2	\	74

Table 7: Statistical Data of Group 2.

Statistical Data									
class	subcategories	template	positive	missing	bulge	crack	twist	total	
cone	4	4	25	11	7	4	8	59	
bowl	4	4	25	10	7	3	7	56	
door	4	4	21	2	4	3	7	41	
keyboard	4	4	24	11	8	4	6	57	
night_stand	4	4	31	5	6	3	6	55	
raido	4	4	25	8	7	4	7	55	
vase	4	4	32	12	8	4	8	68	
xbox	4	4	29	11	8	3	8	63	

Real3D-AD, which may pose challenges in the real industry. Thus, we provide a more comprehensive test benchmark for 3D anomaly detection in the real industry.

D.2 Anomaly Data Synthesis

We collated samples of Anomaly-ShapeNet and used this to generate Group 1 to produce simpler anomaly detection data. Following Anomaly-ShapeNet, we selected some of the categories on ShapeNet [49] as base samples to generate Group 2 and performed manual anomaly generation by using Blender software, commonly used in industry. In a further effort to simulate the noise problem present in industry, we imported Gaussian noise with a variance of 0.002 to simulate environmental and equipment effects. Finally, we labelled the ground truth through CloudCompare.

D.3 Dataset Statistics.

The data contains more than 1,000 samples in 16 categories, four samples in the training set, and dozens of samples in the test set, and the statistics for Group 1 and Group 2 are shown in Tables 6 and 7, respectively. Sample point clouds range from 7,000 to 25,000 points, meeting the scanning accuracy of the actual industry.

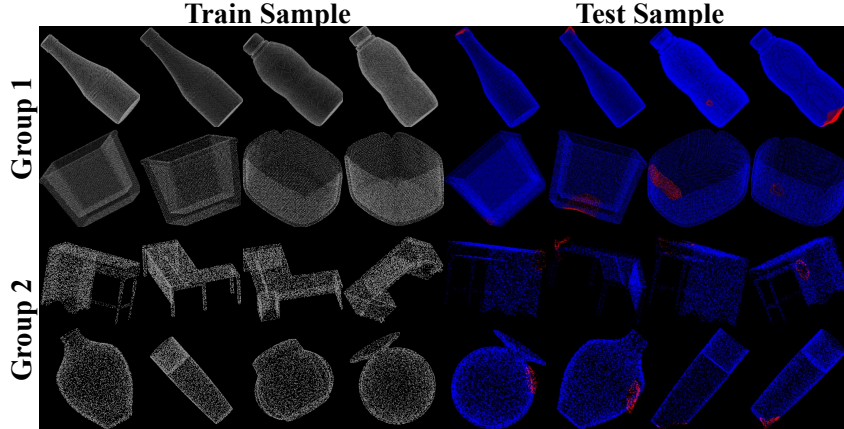


Figure 5: Visualization of the training and test sets on Group 1 and Group 2.

E More Ablation Results

Table 8: More Parameter Sensitivity Analyses.

(a) Parameter Sensitivity Analysis to G .					(b) Parameter Sensitivity Analysis to λ				
Number	16	32	64	128	λ	[0.900,1]	[0.925,1]	[0.950,1]	[0.975,1]
O-AUROC	0.769	0.780	0.786	0.766	O-AUROC	0.759	0.767	0.786	0.780
P-AUROC	0.810	0.812	0.837	0.798	P-AUROC	0.801	0.784	0.837	0.828

(c) Parameter Sensitivity Analysis to σ					(d) Parameter Sensitivity Analysis to γ				
σ	[0,0.02]	[0,0.04]	[0,0.08]	[0,0.16]	γ	[0,0.06]	[0.03,0.09]	[0.06,0.12]	[0.09,0.15]
O-AUROC	0.769	0.780	0.786	0.758	O-AUROC	0.711	0.739	0.786	0.750
P-AUROC	0.814	0.823	0.837	0.801	P-AUROC	0.754	0.788	0.837	0.799

E.1 Parameter Sensitivity Analyses to Patches of Pseudo Anomalies

An appropriate size is essential for learning the features of normal structures. The size of pseudo-abnormal regions is inversely correlated with the patch number G . As in Table 8a, we report the ablation results regarding G . When G was set to 16, the anomaly region was larger, resulting in lower performance, with 1.7% and 2.7% lower O-AUROC and P-AUROC, respectively. The anomalous region was smaller with G set to 128, leading to sub-optimal performance with 2.0% and 3.9% lower O-AUROC and P-AUROC, respectively. This is attributed to distorted pseudo-anomalies due to too large or too small anomalous regions, and we used $G=64$ as a parameter for the comparison experiments.

E.2 Parameter Sensitivity Analyses to DA-Gen

DA-Gen contains three key parameters: λ , σ , and γ . We set a reference value based on empirical evidence and show the results of the parameter sensitivity analyses in Tables 8b, 8c, and 8d, respectively. A smaller λ indicates that the direction in which the anomaly occurs is shifted towards the random direction to a greater extent. When λ was set to a smaller [0.900,1] and larger [0.975, 1] resulted in an average decrease of 1.62% and 2.25% for O-AUROC and P-AUROC, respectively. We select a moderate value $\lambda = [0.950,1]$ to generate the true anomaly. The stretching parameter σ is used to control the degree of narrowing of the anomalous shape. We chose $\sigma = [0,0.08]$ to obtain the best performance for the anomaly detection metrics of 78.6% and 83.7% compared to the performance degradation of 2.25% and 2.95% caused by the narrower $\sigma = [0,0.02]$ and the wider $\sigma = [0,0.16]$. γ represents the maximum displacement magnitude of the center of the anomaly. The γ set to a larger [0.09,0.15] or smaller [0,0.06] resulted in an average decrease in the anomaly detection metrics of

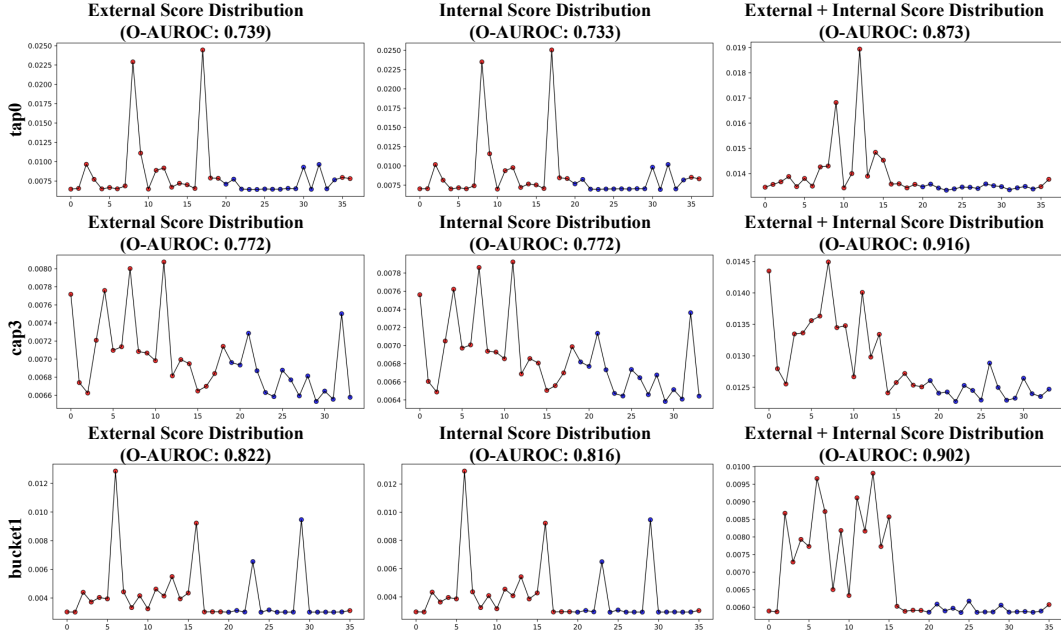


Figure 6: The distribution of anomaly detection scores on different classes, compared between External, Internal, and Internal+External. **Red** and **blue** represent abnormal and normal points, respectively.

5.5% and 6.05%. We choose $\gamma=[0.06,0.12]$ for optimal anomaly creation. We simply visualise the generated point cloud in Appendix F.3.

E.3 Parameter Sensitivity Analyses to HQC

The b represents the $b\%$ of samples with the lowest object-level scores at the time of the first decision that were considered normal. The proper threshold is crucial for performing HQC correctly: too small a threshold leads to insignificant improvement in inference speed, and too large a threshold leads to performance degradation. The parameter sensitivity analyses to the thresholds are displayed in Table 9. When b is set to 0.15, the efficiency gain is insignificant. When set to 0.35, its O-AUROC and P-AUROC performance decreases by 4.5% and 4.4%, respectively. when a is set to 0.25, the performance and efficiency of the experiment are balanced.

Table 9: Parameter Sensitivity Analysis to b .

b	0.150	0.200	0.250	0.300	0.350
O-AUROC	0.790	0.783	0.790	0.779	0.745
P-AUROC	0.837	0.835	0.837	0.820	0.793
FPS	14.7	15.1	15.7	16.1	16.9

F More Visualisation Results

F.1 The Distribution of Scores

We show more distributions of Scores in Figure 6. The model is better able to reduce anomalies when both corrective forces are applied at the same time, e.g., the detection performance of the “tap0” class is 73.9% and 73.3% respectively, without the use of the resultant force, and the detection performance rises to 87.3% when applied together. This is attributed to the fact that anomalies in real manufacturing processes often originate from a combination of internal and external influences.

F.2 Qualitative Results of Detection

We show more visualisations in Figure 8 and 9. Our model successfully localises anomalies and assigns a lower anomaly score to normal structures.

F.3 Visualisations of DA-Gen

The realistic pseudo-anomalies facilitate our CFP-Net to capture the potential damaging forces of anomalous structures and generate corrective forces to restore the anomalies. We show the generated anomaly samples with real anomaly samples in Figure 7. Our method generates anomalies close to the real ones.

G More Experimental Results

We show the P-AUROC and O-AUROC results for Anomaly-ShapeNet in Table 11 and Table 10, respectively. We show the P-AUROC results for Anomaly-ShapeNet-New in Table 13. In Table 17 we show Real3D-AD for P-AUROC.

We obtained the best results in all metrics. As shown in Table 16, we show Mvtec-AD for P-AUROC. We obtained the best results in all metrics.

H Limitations and Feature Work

We discuss further limitations in this section and point the direction of future work. Our framework lacks explicit physical constraints. Current approaches in the robotics area incorporating physical engines [60] (e.g., LLM-based priors) face challenges in 3D anomaly detection, primarily due to the inherent structural ambiguity of 3D point clouds and the non-physical randomization in synthetic dataset generation. Notably, real-world benchmarks we use like Real3D-AD [5] and MvTec3D-AD [43] maintain authentic physical constraints. Future dataset development should integrate comprehensive physical descriptors (e.g., RGB textures, illumination conditions, and industrial contexts) to enable explicit physical regularization in anomaly detection models.

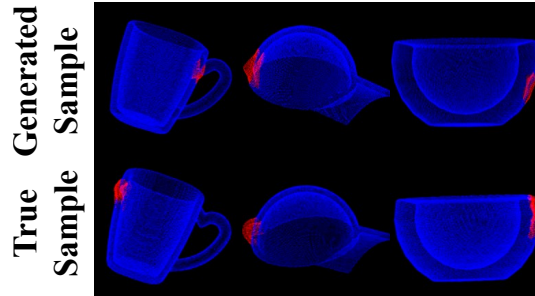


Figure 7: Qualitative results of localization.

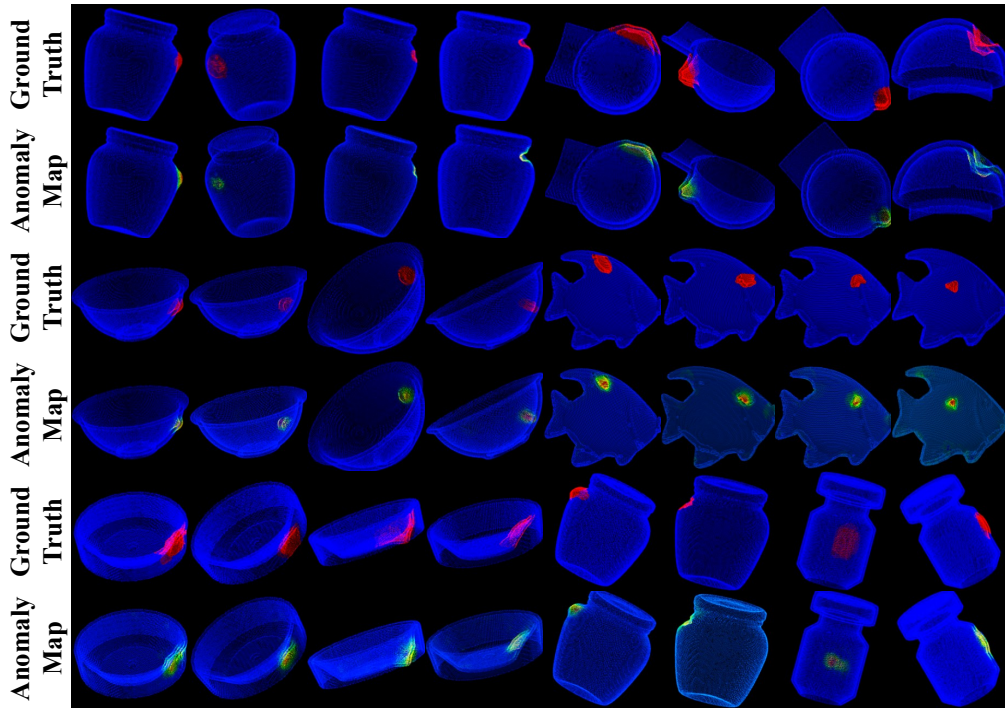


Figure 8: More qualitative results of localization.

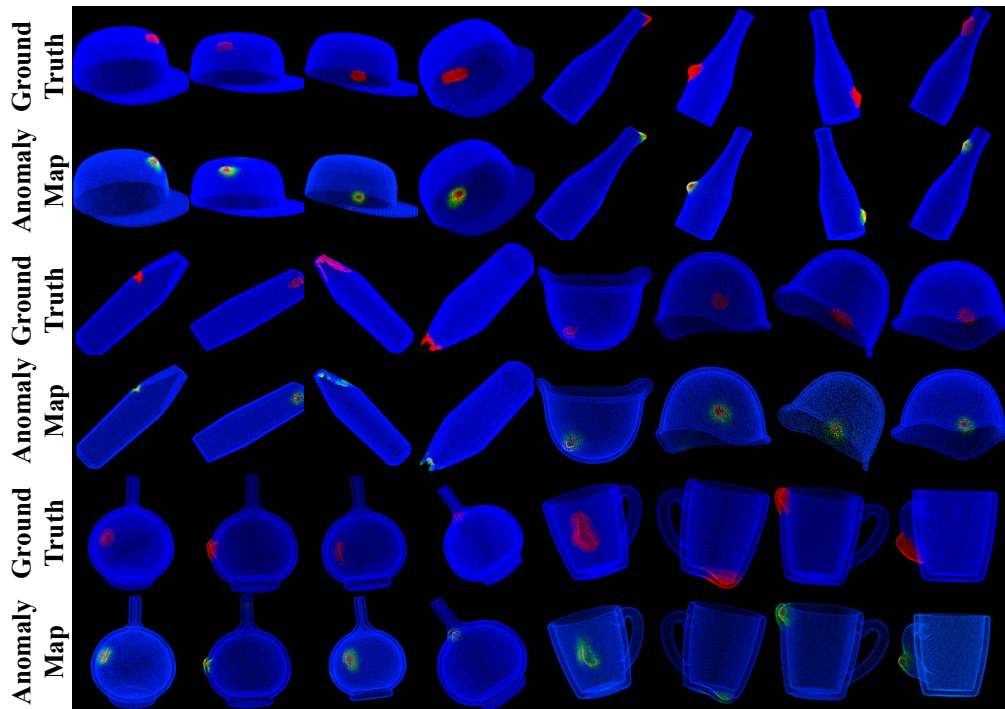


Figure 9: More qualitative results of localization.

Table 10: O-AUROC performance of different methods on Anomaly-ShapeNet across 40 categories, where best and second-place results are highlighted in **red** and **blue**, respectively.

O-AUROC														
Method	ashtray0	bag0	bottle0	bottle1	bottle3	bow0	bow1	bow2	bow3	bow4	bow5	bucket0	bucket1	cap0
BTF(Raw)(CVPR23 [*])	0.578	0.410	0.597	0.510	0.568	0.564	0.264	0.525	0.385	0.664	0.417	0.617	0.321	0.668
BTF(FPFH)(CVPR23 [*])	0.420	0.546	0.344	0.546	0.322	0.509	0.668	0.510	0.490	0.609	0.699	0.401	0.633	0.618
M3DM(CVPR23 [*])	0.577	0.537	0.574	0.637	0.541	0.634	0.663	0.684	0.617	0.464	0.409	0.309	0.501	0.557
PatchCore(FPFH)(CVPR22 [*])	0.587	0.571	0.604	0.667	0.572	0.504	0.639	0.615	0.537	0.494	0.558	0.469	0.551	0.580
PatchCore(PointMAE)(CVPR22 [*])	0.591	0.601	0.513	0.601	0.650	0.523	0.629	0.458	0.579	0.501	0.593	0.593	0.561	0.589
CPMF(PR24 [*])	0.353	0.643	0.520	0.482	0.405	0.783	0.639	0.625	0.658	0.683	0.685	0.482	0.601	0.601
Reg3D-AD(NeurIPS23 [*])	0.597	0.706	0.486	0.695	0.525	0.671	0.525	0.490	0.348	0.663	0.593	0.610	0.752	0.693
IMRNet(CVPR24 [*])	0.671	0.660	0.552	0.700	0.640	0.681	0.702	0.685	0.599	0.676	0.710	0.580	0.771	0.737
R3D-AD(ECCV24 [*])	0.833	0.720	0.733	0.737	0.781	0.819	0.778	0.741	0.767	0.744	0.656	0.683	0.756	0.822
PO3AD(CVPR25 [*])	1.000	0.833	0.900	0.933	0.926	0.922	0.829	0.833	0.881	0.981	0.849	0.853	0.787	0.877
Ours	1.000	0.976	0.957	1.000	0.956	0.985	0.904	0.919	0.937	0.996	0.919	0.943	0.902	0.878
Method	cap3	cap4	cap5	cup0	cup1	eraser0	headset0	headset1	helmet0	helmet1	helmet2	helmet3	jar0	micro.0
BTF(Raw)(CVPR23 [*])	0.527	0.468	0.373	0.403	0.521	0.525	0.378	0.515	0.553	0.349	0.602	0.526	0.420	0.623
BTF(FPFH)(CVPR23 [*])	0.522	0.520	0.586	0.586	0.610	0.719	0.520	0.490	0.571	0.719	0.542	0.444	0.424	0.671
M3DM(CVPR23 [*])	0.423	0.777	0.639	0.539	0.556	0.627	0.577	0.617	0.526	0.427	0.623	0.374	0.441	0.357
PatchCore(FPFH)(CVPR22 [*])	0.453	0.757	0.790	0.600	0.586	0.657	0.583	0.637	0.546	0.484	0.425	0.404	0.472	0.388
PatchCore(PointMAE)(CVPR22 [*])	0.476	0.727	0.538	0.610	0.556	0.677	0.591	0.627	0.556	0.552	0.447	0.424	0.483	0.488
CPMF(PR24 [*])	0.551	0.553	0.697	0.497	0.499	0.689	0.643	0.458	0.555	0.589	0.462	0.520	0.610	0.509
Reg3D-AD(NeurIPS23 [*])	0.725	0.643	0.467	0.510	0.538	0.343	0.537	0.610	0.600	0.381	0.614	0.367	0.592	0.414
IMRNet(CVPR24 [*])	0.775	0.652	0.652	0.643	0.757	0.548	0.720	0.676	0.597	0.600	0.641	0.573	0.780	0.755
R3D-AD(ECCV24 [*])	0.730	0.681	0.670	0.776	0.757	0.890	0.738	0.795	0.757	0.720	0.633	0.707	0.838	0.762
PO3AD(CVPR25 [*])	0.859	0.792	0.670	0.871	0.833	0.808	0.923	0.762	0.964	0.869	0.754	0.869	0.776	0.776
Ours	0.916	0.835	0.818	0.990	0.938	1.000	0.884	0.990	0.841	0.986	0.962	0.803	0.914	0.924
Method	shelf0	tap0	tap1	vase0	vase1	vase2	vase3	vase4	vase5	vase7	vase8	vase9	Average	Mean Rank
BTF(Raw)(CVPR23 [*])	0.164	0.525	0.573	0.531	0.549	0.410	0.717	0.425	0.585	0.448	0.424	0.564	0.493	8.725
BTF(FPFH)(CVPR23 [*])	0.609	0.560	0.546	0.342	0.219	0.546	0.699	0.510	0.409	0.518	0.668	0.268	0.528	8.025
M3DM(CVPR23 [*])	0.564	0.754	0.739	0.423	0.427	0.737	0.439	0.476	0.317	0.657	0.663	0.663	0.552	7.825
PatchCore(FPFH)(CVPR22 [*])	0.494	0.753	0.766	0.455	0.423	0.721	0.449	0.506	0.417	0.693	0.662	0.660	0.568	7.350
PatchCore(PointMAE)(CVPR22 [*])	0.523	0.458	0.538	0.447	0.552	0.741	0.460	0.516	0.579	0.650	0.663	0.629	0.562	7.400
CPMF(PR24 [*])	0.685	0.359	0.697	0.451	0.345	0.582	0.582	0.514	0.618	0.397	0.529	0.609	0.559	7.350
Reg3D-AD(NeurIPS23 [*])	0.688	0.676	0.641	0.533	0.702	0.605	0.650	0.500	0.520	0.462	0.620	0.594	0.572	7.450
IMRNet(CVPR24 [*])	0.603	0.676	0.696	0.533	0.757	0.614	0.700	0.524	0.676	0.635	0.630	0.594	0.661	4.950
R3D-AD(ECCV24 [*])	0.696	0.736	0.900	0.788	0.729	0.752	0.742	0.630	0.757	0.771	0.721	0.718	0.749	3.225
PO3AD(CVPR25 [*])	0.573	0.745	0.681	0.858	0.742	0.952	0.821	0.675	0.852	0.966	0.739	0.830	0.839	2.350
Ours	0.696	0.873	0.700	0.983	0.838	0.976	0.848	0.755	0.910	0.967	0.818	0.909	0.909	1.075

Table 11: P-AUROC performance of different methods on Anomaly-ShapeNet across 40 categories, where best and second-place results are highlighted in **red** and **blue**, respectively.

P-AUROC														
Method	ashtray0	bag0	bottle0	bottle1	bottle3	bow0	bow1	bow2	bow3	bow4	bow5	bucket0	bucket1	cap0
BTF(Raw)(CVPR23 [*])	0.512	0.430	0.551	0.491	0.720	0.524	0.464	0.426	0.685	0.563	0.517	0.617	0.686	0.524
BTF(FPFH)(CVPR23 [*])	0.624	0.746	0.641	0.549	0.622	0.710	0.768	0.518	0.590	0.679	0.699	0.401	0.633	0.730
M3DM(CVPR23 [*])	0.577	0.637	0.663	0.637	0.532	0.658	0.663	0.694	0.657	0.624	0.489	0.698	0.699	0.531
PatchCore(FPFH)(CVPR22 [*])	0.597	0.574	0.654	0.687	0.512	0.524	0.531	0.625	0.327	0.720	0.358	0.459	0.571	0.472
PatchCore(PointMAE)(CVPR22 [*])	0.495	0.674	0.553	0.606	0.653	0.527	0.524	0.515	0.581	0.501	0.562	0.586	0.574	0.544
CPMF(PR24 [*])	0.615	0.655	0.521	0.571	0.435	0.745	0.488	0.635	0.641	0.683	0.684	0.486	0.601	0.601
Reg3D-AD(NeurIPS23 [*])	0.698	0.715	0.886	0.696	0.525	0.775	0.615	0.593	0.654	0.800	0.691	0.619	0.752	0.632
IMRNet(CVPR24 [*])	0.671	0.668	0.556	0.702	0.641	0.781	0.705	0.684	0.599	0.576	0.715	0.585	0.774	0.715
ISMNet(AAI25 [*])	0.865	0.734	0.722	0.869	0.740	0.762	0.702	0.706	0.851	0.753	0.733	0.545	0.683	0.672
PO3AD(CVPR25 [*])	0.962	0.949	0.912	0.844	0.880	0.978	0.914	0.918	0.935	0.967	0.941	0.755	0.899	0.957
Ours	0.904	0.957	0.942	0.881	0.896	0.977	0.921	0.965	0.937	0.993	0.952	0.792	0.925	0.959
Method	cap3	cap4	cap5	cup0	cup1	eraser0	headset0	headset1	helmet0	helmet1	helmet2	helmet3	jar0	micro.0
BTF(Raw)(CVPR23 [*])	0.687	0.469	0.373	0.632	0.561	0.637	0.578	0.475	0.504	0.449	0.605	0.700	0.423	0.583
BTF(FPFH)(CVPR23 [*])	0.658	0.524	0.586	0.790	0.619	0.719	0.620	0.591	0.575	0.749	0.643	0.724	0.427	0.675
M3DM(CVPR23 [*])	0.605	0.718	0.655	0.715	0.556	0.710	0.581	0.585	0.599	0.427	0.623	0.655	0.541	0.358
PatchCore(FPFH)(CVPR22 [*])	0.653	0.595	0.795	0.655	0.596	0.810	0.583	0.464	0.489	0.455	0.737	0.478	0.478	0.488
PatchCore(PointMAE)(CVPR22 [*])	0.488	0.725	0.545	0.510	0.856	0.738	0.575	0.423	0.580	0.562	0.651	0.615	0.487	0.886
CPMF(PR24 [*])	0.551	0.553	0.551	0.497	0.509	0.689	0.699	0.458	0.555	0.542	0.515	0.520	0.611	0.545
Reg3D-AD(NeurIPS23 [*])	0.718	0.815	0.467	0.685	0.698	0.755	0.580	0.626	0.600	0.624	0.825	0.620	0.599	0.599
IMRNet(CVPR24 [*])	0.706	0.753	0.742	0.643	0.688	0.548	0.705	0.476	0.598	0.604	0.644	0.663	0.765	0.742
ISMNet(AAI25 [*])	0.775	0.661	0.770	0.552	0.851	0.524	0.472	0.843	0.615	0.603	0.568	0.522	0.661	0.600
PO3AD(CVPR25 [*])	0.948	0.940	0.864	0.909	0.932	0.974	0.823	0.907	0.878	0.948	0.932	0.846	0.871	0.810
Ours	0.946	0.940	0.925	0.917	0.920	0.951	0.780	0.932	0.885	0.926	0.874	0.879	0.877	0.833
Method	shelf0	tap0	tap1	vase0	vase1	vase2	vase3	vase4	vase5	vase7	vase8	vase9	Average	Mean Rank
BTF(Raw)(CVPR23 [*])	0.464	0.527	0.564	0.618	0.549	0.403	0.602	0.613	0.585	0.578	0.550	0.564	0.550	8.675
BTF(FPFH)(CVPR23 [*])	0.619	0.568	0.596	0.642	0.619	0.646	0.699	0.710	0.429	0.540	0.662	0.568	0.628	6.525
M3DM(CVPR23 [*])	0.554	0.654	0.712	0.608	0.602	0.737	0.658	0.655	0.642	0.517	0.551	0.663	0.616	6.850
PatchCore(FPFH)(CVPR22 [*])	0.613	0.733	0.768	0.655	0.453	0.721	0.430	0.505	0.447	0.693	0.575	0.663	0.580	7.800
PatchCore(PointMAE)(CVPR22 [*])	0.543	0.858	0.541	0.677	0.551	0.742	0.465	0.523	0.572	0.651	0.364	0.423	0.577	7.950
CPMF(PR24 [*])	0.783	0.458	0.657	0.458	0.486	0.582	0.582	0.514	0.651	0.504	0.529	0.545	0.573	8.450
Reg3D-AD(NeurIPS23 [*])	0.688	0.589	0.741	0.548	0.602	0.405	0.511	0.755	0.624	0.881	0.811	0.694	0.668	5.375
IMRNet(CVPR24 [*])	0.605	0.681	0.699	0.535	0.685	0.614	0.401	0.524	0.682	0.593	0.635	0.691	0.650	5.800
ISMNet(AAI25 [*])	0.701	0.844	0.678	0.687	0.534	0.773	0.622	0.546	0.580	0.747	0.736	0.823	0.691	5.150
PO3AD(CVPR25 [*])	0.663	0.783	0.692	0.955	0.882	0.978	0.884	0.902	0.937	0.982	0.950	0.952	0.898	1.975
Ours	0.810	0.798	0.777	0.969	0.889	0.990	0.882							

Table 12: O-AUPR performance of different methods on Anomaly-ShapeNet across 40 categories, where best and second-place results are highlighted in **red** and **blue**, respectively.

O-AUPR														
Method	ashtray0	bag0	bottle0	bottle1	bottle3	bow0	bow1	bow2	bow3	bow4	bow5	bucket0	bucket1	cap0
BTF(Raw)(CVPR23 [*])	0.578	0.458	0.466	0.573	0.543	0.588	0.464	0.576	0.654	0.601	0.615	0.652	0.620	0.659
BTF(FPFH)(CVPR23 [*])	0.651	0.551	0.644	0.625	0.602	0.576	0.648	0.515	0.499	0.632	0.699	0.483	0.648	0.618
M3DM(CVPR23 [*])	0.632	0.642	0.763	0.674	0.451	0.525	0.515	0.630	0.635	0.571	0.601	0.609	0.507	0.564
PatchCore(FPFH)(CVPR22 [*])	0.445	0.608	0.615	0.677	0.579	0.548	0.545	0.611	0.620	0.575	0.541	0.604	0.565	0.585
PatchCore(PointMAE)(CVPR22 [*])	0.679	0.601	0.545	0.645	0.651	0.562	0.611	0.456	0.556	0.601	0.585	0.541	0.642	0.561
CPMF(PR24 [*])	0.453	0.655	0.588	0.592	0.505	0.775	0.621	0.601	0.418	0.683	0.685	0.662	0.501	0.601
Reg3D-AD(NeurIPS23 [*])	0.588	0.608	0.632	0.695	0.474	0.494	0.515	0.495	0.441	0.624	0.555	0.632	0.714	0.693
IMRNet(CVPR24 [*])	0.612	0.665	0.558	0.702	0.648	0.481	0.504	0.681	0.614	0.630	0.652	0.578	0.732	0.711
PO3AD(CVPR25 [*])	0.999	0.809	0.927	0.959	0.962	0.946	0.905	0.888	0.927	0.985	0.904	0.923	0.882	0.841
Ours	1.000	0.981	0.972	1.000	0.974	0.990	0.937	0.949	0.962	0.997	0.950	0.971	0.936	0.932
Method	cap3	cap4	cap5	cup0	cup1	eraser0	headset0	headset1	helmet0	helmet1	helmet2	helmet3	jar0	micro.0
BTF(Raw)(CVPR23 [*])	0.612	0.515	0.653	0.601	0.701	0.425	0.379	0.515	0.559	0.388	0.615	0.526	0.428	0.613
BTF(FPFH)(CVPR23 [*])	0.579	0.545	0.593	0.585	0.651	0.719	0.531	0.523	0.568	0.721	0.588	0.564	0.479	0.662
M3DM(CVPR23 [*])	0.652	0.477	0.684	0.570	0.752	0.625	0.632	0.623	0.528	0.627	0.636	0.458	0.555	0.464
PatchCore(FPFH)(CVPR22 [*])	0.457	0.655	0.725	0.604	0.586	0.584	0.701	0.601	0.525	0.630	0.475	0.494	0.499	0.332
PatchCore(PointMAE)(CVPR22 [*])	0.583	0.721	0.542	0.642	0.710	0.801	0.515	0.423	0.633	0.571	0.496	0.611	0.463	0.652
CPMF(PR24 [*])	0.541	0.645	0.697	0.647	0.609	0.544	0.602	0.619	0.333	0.501	0.477	0.645	0.618	0.655
Reg3D-AD(NeurIPS23 [*])	0.711	0.623	0.770	0.531	0.638	0.424	0.538	0.617	0.600	0.381	0.618	0.468	0.601	0.614
IMRNet(CVPR24 [*])	0.702	0.658	0.502	0.455	0.627	0.599	0.701	0.656	0.697	0.615	0.602	0.575	0.760	0.552
PO3AD(CVPR25 [*])	0.906	0.876	0.801	0.879	0.870	0.995	0.765	0.914	0.864	0.961	0.934	0.849	0.915	0.803
Ours	0.939	0.902	0.897	0.991	0.937	1.000	0.872	0.991	0.892	0.987	0.980	0.891	0.918	0.933
Method	shelf0	tap0	tap1	vase0	vase1	vase2	vase3	vase4	vase5	vase7	vase8	vase9	Average	Mean Rank
BTF(Raw)(CVPR23 [*])	0.624	0.535	0.594	0.562	0.441	0.413	0.717	0.428	0.615	0.547	0.416	0.482	0.549	7.525
BTF(FPFH)(CVPR23 [*])	0.611	0.610	0.575	0.641	0.655	0.569	0.652	0.587	0.472	0.592	0.624	0.638	0.598	6.350
M3DM(CVPR23 [*])	0.665	0.722	0.638	0.788	0.652	0.615	0.551	0.526	0.633	0.648	0.463	0.651	0.603	6.175
PatchCore(FPFH)(CVPR22 [*])	0.504	0.712	0.684	0.645	0.623	0.801	0.481	0.777	0.515	0.621	0.515	0.660	0.588	6.675
PatchCore(PointMAE)(CVPR22 [*])	0.543	0.712	0.542	0.548	0.572	0.711	0.455	0.586	0.585	0.652	0.655	0.634	0.595	6.625
CPMF(PR24 [*])	0.681	0.639	0.697	0.632	0.645	0.632	0.588	0.655	0.518	0.432	0.673	0.618	0.597	6.175
Reg3D-AD(NeurIPS23 [*])	0.675	0.676	0.599	0.615	0.468	0.641	0.651	0.505	0.588	0.455	0.629	0.574	0.584	6.675
IMRNet(CVPR24 [*])	0.625	0.401	0.796	0.573	0.725	0.655	0.708	0.528	0.654	0.601	0.639	0.462	0.621	5.600
PO3AD(CVPR25 [*])	0.680	0.856	0.709	0.753	0.789	0.963	0.902	0.824	0.879	0.971	0.833	0.904	0.881	2.050
Ours	0.829	0.923	0.801	0.984	0.886	0.981	0.917	0.838	0.922	0.971	0.906	0.941	0.940	1.000

Table 13: P-AUROC performance of different methods on Anomaly-ShapeNet-New across 12 categories, where best and second-place results are highlighted in **red** and **blue**, respectively.

P-AUROC														
Method	cabinet0	cap0	cap2	chair0	cup2	desk0	knife0	knife1	micro.1	screen0	vase10	vase6	Average	Mean Rank
BTF(Raw)(CVPR23 [*])	0.464	0.640	0.600	0.508	0.492	0.611	0.486	0.433	0.505	0.548	0.439	0.453	0.515	6.667
BTF(FPFH)(CVPR23 [*])	0.725	0.915	0.722	0.653	0.843	0.864	0.736	0.774	0.888	0.720	0.741	0.896	0.790	3.250
M3DM(CVPR23 [*])	0.642	0.754	0.750	0.532	0.657	0.587	0.507	0.601	0.768	0.613	0.696	0.668	0.648	4.750
PatchCore(FPFH)(CVPR22 [*])	0.979	0.966	0.725	0.852	0.959	0.979	0.855	0.935	0.992	0.939	0.948	0.950	0.923	1.917
PatchCore(PointMAE)(CVPR22 [*])	0.675	0.755	0.757	0.570	0.686	0.590	0.499	0.546	0.717	0.590	0.672	0.681	0.645	4.667
Reg3D-AD(NeurIPS23 [*])	0.629	0.773	0.747	0.494	0.631	0.599	0.488	0.569	0.704	0.613	0.667	0.656	0.631	5.417
Ours	0.988	0.992	0.843	0.911	0.948	0.989	0.866	0.904	0.920	0.976	0.933	0.968	0.937	1.333

Table 14: O-AUROC performance of different methods on Anomaly-ShapeNet-New across 12 categories, where best and second-place results are highlighted in **red** and **blue**, respectively.

O-AUROC														
Method	cabinet0	cap0	cap2	chair0	cup2	desk0	knife0	knife1	micro.1	screen0	vase10	vase6	Average	Mean Rank
BTF(Raw)(CVPR23 [*])	0.490	0.544	0.330	0.357	0.562	0.500	0.393	0.503	0.492	0.533	0.620	0.670	0.500	5.917
BTF(FPFH)(CVPR23 [*])	0.773	0.761	0.596	0.533	0.486	0.503	0.550	0.657	0.837	0.419	0.788	0.676	0.632	4.250
M3DM(CVPR23 [*])	0.613	0.625	0.435	0.543	0.667	0.580	0.487	0.507	0.483	0.663	0.612	0.667	0.574	4.583
PatchCore(FPFH)(CVPR22 [*])	1.000	0.944	0.870	0.903	0.962	0.967	0.863	0.720	0.917	0.667	0.948	0.848	0.884	1.500
PatchCore(PointMAE)(CVPR22 [*])	0.440	0.667	0.565	0.577	0.619	0.543	0.490	0.490	0.517	0.656	0.617	0.709	0.574	4.333
Reg3D-AD(NeurIPS23 [*])	0.610	0.585	0.505	0.533	0.495	0.510	0.460	0.473	0.475	0.552	0.565	0.630	0.533	5.917
Ours	0.904	0.933	0.865	0.898	0.932	1.000	0.894	0.800	0.854	0.718	1.000	0.859	0.888	1.500

Table 15: O-AUROC performance of different methods on only-3D MvTec3D-AD across 10 categories, where best and second-place results are highlighted in **red** and **blue**, respectively.

O-AUROC													
Method	Bagel	Cable Gland	Carrot	Cookie	Dowel	Foam	Peach	Potato	Rope	Tire	Average	Mean Rank	
BTF(CVPR23 [*])	0.825	0.551	0.952	0.797	0.883	0.582	0.758	0.889	0.929	0.653	0.782	6.400	
EasyNet(MM23 [*])	0.629	0.716	0.768	0.731	0.660	0.710	0.712	0.711	0.688	0.731	0.706	7.100	
M3DM(CVPR23 [*])	0.941	0.651	0.965	0.969	0.905	0.760	0.880	0.974	0.926	0.765	0.874	4.400	
AST(WACV23 [*])	0.881	0.576	0.965	0.957	0.679	0.797	0.990	0.915	0.956	0.611	0.833	4.900	
Shape-Guided(ICML23 [*])	0.983	0.682	0.978	0.998	0.960	0.737	0.993	0.979	0.966	0.871	0.915	2.600	
CFM(CVPR24 [*])	\	\	\	\	\	\	\	\	\	\	0.816	\	
CPMF(PR24 [*])	0.983	0.889	0.989	0.991	0.958	0.809	0.988	0.959	0.979	0.969	0.951	2.200	
3D-ADNAS(AAAI25 [*])	0.794	0.656	0.859	0.795	0.780	0.629	0.843	0.781	0.824	0.878	0.784	6.200	
Ours	0.990	0.922	0.965	0.979	0.970	0.841	0.952	0.983	0.982	0.951	0.954	1.800	

Table 16: P-AUROC performance of different only-3D methods on MvTec3D-AD across 10 categories, where best and second-place results are highlighted in **red** and **blue**, respectively.

P-AUROC												
Method	Bagel	Cable Gland	Carrot	Cookie	Dowel	Foam	Peach	Potato	Rope	Tire	Average	Mean Rank
BTF (CVPR23 [*])	0.973	0.879	0.982	0.906	0.892	0.735	0.977	0.982	0.956	0.961	0.924	4.800
M3DM (CVPR23 [*])	0.943	0.818	0.977	0.882	0.881	0.743	0.958	0.974	0.950	0.929	0.906	6.900
Shape-Guided (ICML23 [*])	0.974	0.871	0.981	0.924	0.898	0.773	0.978	0.983	0.955	0.969	0.931	3.800
CPMF (PR24 [*])	0.958	0.946	0.979	0.868	0.897	0.746	0.980	0.981	0.961	0.977	0.929	4.300
MMRD (AAAI24 [*])	0.926	0.806	0.965	0.858	0.904	0.731	0.962	0.958	0.966	0.936	0.901	6.600
3DSR (WACV24 [*])	0.922	0.872	0.984	0.859	0.940	0.714	0.970	0.978	0.977	0.958	0.907	5.000
LSFA (ECCV24 [*])	0.974	0.887	0.981	0.921	0.901	0.773	0.982	0.983	0.959	0.981	0.934	2.900
Ours	0.976	0.931	0.983	0.928	0.908	0.784	0.985	0.991	0.984	0.988	0.946	1.300

Table 17: P-AUROC performance of different methods on Real3D-AD across 12 categories, where best and second-place results are highlighted in **red** and **blue**, respectively.

P-AUROC														
Method	Airplane	Car	Candy	Chicken	Diamond	Duck	Fish	Gemstone	Seahorse	Shell	Starfish	Toffees	Mean	Mean Rank
BTF(Raw) (CVPR23 [*])	0.564	0.647	0.735	0.609	0.563	0.601	0.514	0.597	0.520	0.489	0.392	0.623	0.571	7.417
BTF(FPFH) (CVPR23 [*])	0.738	0.708	0.864	0.735	0.882	0.875	0.709	0.891	0.512	0.571	0.501	0.815	0.733	4.417
M3DM (CVPR23 [*])	0.547	0.602	0.679	0.678	0.608	0.667	0.606	0.674	0.560	0.738	0.532	0.682	0.631	6.417
PatchCore(FPFH) (CVPR22 [*])	0.562	0.754	0.780	0.429	0.828	0.264	0.829	0.910	0.739	0.739	0.606	0.747	0.682	5.000
PatchCore(PointMAE) (CVPR22 [*])	0.569	0.609	0.627	0.729	0.718	0.528	0.717	0.444	0.633	0.709	0.580	0.580	0.620	6.417
Reg3D-AD (NeurIPS23 [*])	0.631	0.718	0.724	0.676	0.835	0.503	0.826	0.545	0.817	0.811	0.617	0.759	0.705	4.667
R3D-AD (ECCV24 [*])	0.594	0.557	0.593	0.620	0.555	0.635	0.573	0.668	0.562	0.578	0.608	0.568	0.592	7.000
ISMIP (AAAI25 [*])	0.753	0.836	0.907	0.798	0.926	0.876	0.886	0.857	0.813	0.839	0.641	0.895	0.836	1.917
Ours	0.792	0.839	0.842	0.850	0.844	0.780	0.934	0.892	0.820	0.869	0.792	0.784	0.837	1.750

Table 18: O-AUROC performance of different methods on Real3D-AD across 12 categories, where best and second-place results are highlighted in **red** and **blue**, respectively.

O-AUROC														
Method	Airplane	Car	Candy	Chicken	Diamond	Duck	Fish	Gemstone	Seahorse	Shell	Starfish	Toffees	Average	Mean Rank
BTF(Raw) (CVPR23 [*])	0.730	0.647	0.539	0.789	0.707	0.691	0.602	0.686	0.596	0.396	0.530	0.703	0.635	7.583
BTF(FPFH) (CVPR23 [*])	0.520	0.560	0.630	0.432	0.545	0.784	0.549	0.648	0.779	0.754	0.575	0.462	0.603	7.833
M3DM (CVPR23 [*])	0.434	0.541	0.552	0.683	0.602	0.433	0.540	0.644	0.495	0.694	0.551	0.450	0.552	9.833
PatchCore(FPFH) (CVPR22 [*])	0.882	0.590	0.541	0.837	0.574	0.546	0.675	0.370	0.505	0.589	0.441	0.565	0.593	8.417
PatchCore(PointMAE) (CVPR22 [*])	0.726	0.498	0.663	0.827	0.783	0.489	0.630	0.374	0.539	0.501	0.519	0.585	0.594	8.750
CPMF (PR24 [*])	0.701	0.551	0.552	0.504	0.523	0.582	0.558	0.589	0.729	0.653	0.700	0.390	0.586	8.833
Reg3D-AD (NeurIPS23 [*])	0.716	0.697	0.685	0.852	0.900	0.584	0.915	0.417	0.762	0.583	0.506	0.827	0.704	5.500
IMRNet (CVPR24 [*])	0.762	0.711	0.755	0.780	0.905	0.517	0.880	0.674	0.604	0.665	0.674	0.774	0.725	5.000
R3D-AD (ECCV24 [*])	0.772	0.696	0.713	0.714	0.685	0.909	0.692	0.665	0.720	0.840	0.701	0.703	0.734	4.750
ISMIP (AAAI25 [*])	0.858	0.731	0.852	0.714	0.948	0.712	0.945	0.468	0.729	0.623	0.660	0.842	0.757	3.917
PO3AD (CVPR25 [*])	0.804	0.654	0.785	0.686	0.801	0.820	0.859	0.693	0.756	0.800	0.758	0.771	0.765	4.167
Ours	0.871	0.684	0.811	0.701	0.836	0.824	0.890	0.701	0.754	0.803	0.770	0.785	0.786	3.083

Table 19: O-AUROC and P-AUROC performances of different methods on Anomaly-IntraVariance across 16 categories, where best and second-place results are highlighted in **red** and **blue**, respectively.

Group 1 (two subcategories)																		
Method	O-AUROC								P-AUROC									
	bucket	micro	cup	tap	bottle	helmet	cap	bowl	Average	bucket	micro	cup	tap	bottle	helmet	cap	bowl	Average
BTF (Raw)	0.486	0.524	0.530	0.493	0.522	0.592	0.439	0.544	0.516	0.498	0.553	0.520	0.486	0.571	0.520	0.458	0.465	0.509
BTF (FPFH)	0.473	0.723	0.500	0.587	0.680	0.433	0.661	0.700	0.595	0.730	0.831	0.811	0.606	0.684	0.702	0.936	0.786	0.761
M3DM (PointMAE)	0.555	0.592	0.506	0.436	0.624	0.500	0.533	0.563	0.539	0.537	0.714	0.588	0.494	0.663	0.561	0.662	0.589	0.601
PatchCore (FPFH)	0.688	0.838	0.692	0.533	0.808	0.588	0.941	0.807	0.737	0.803	0.869	0.830	0.594	0.668	0.743	0.971	0.919	0.800
Reg3D-AD	0.449	0.574	0.479	0.530	0.585	0.470	0.537	0.616	0.530	0.491	0.660	0.610	0.491	0.607	0.578	0.656	0.590	0.585
PO3AD	0.699	0.748	0.722	0.609	0.785	0.602	0.680	0.776	0.703	0.649	0.748	0.801	0.594	0.701	0.668	0.912	0.889	0.745
Ours	0.740	0.722	0.739	0.711	0.843	0.688	0.842	0.800	0.761	0.813	0.766	0.899	0.654	0.712	0.722	0.948	0.940	0.807

Group 2 (four subcategories)																		
Method	O-AUROC								P-AUROC									
	xbox	vase	radio	night_stand	keyboard	door	desk	cone	Average	xbox	vase	radio	night_stand	keyboard	door	desk	cone	Average
BTF (Raw)	0.040	0.125	0.023	0.011	0.042	0.011	0.006	0.030	0.036	0.285	0.413	0.448	0.363	0.314	0.234	0.305	0.347	0.339
BTF (FPFH)	0.436	0.430	0.340	0.415	0.418	0.504	0.597	0.587	0.466	0.556	0.515	0.588	0.528	0.424	0.515	0.452	0.577	0.519
M3DM (PointMAE)	0.046	0.258	0.417	0.121	0.161	0.068	0.190	0.015	0.160	0.350	0.487	0.582	0.341	0.369	0.299	0.342	0.437	0.401
PatchCore (FPFH)	0.309	0.573	0.425	0.534	0.559	0.449	0.402	0.675	0.491	0.702	0.592	0.626	0.550	0.448	0.507	0.491	0.570	0.561
Reg3D-AD	0.225	0.616	0.308	0.390	0.066	0.008	0.449	0.565	0.328	0.491	0.660	0.610	0.491	0.607	0.578	0.656	0.590	0.585
PO3AD	0.573	0.728	0.544	0.602	0.504	0.598	0.488	0.720	0.595	0.724	0.608	0.701	0.528	0.611	0.588	0.694	0.601	0.632
Ours	0.612	0.780	0.557	0.594	0.558	0.641	0.602	0.658	0.625	0.795	0.667	0.694	0.643	0.674	0.612	0.714	0.622	0.678